The Astrophysical Journal Letters, 1000:L16 (21pp), 2026 March 20 https://doi.org/10.3847/2041-8213/ae434c


# exoALMA. XXIII. Estimating Disk and Planet Properties from Dust Morphologies with DBNets 2.0

Alessandro Ruzza[1], Giuseppe Lodato[1], Giovanni Rosotti[1], Philip Armitage[2,3], Stefano Facchini[1], Sean M. Andrews[4], Jaehan Bae[5], Marcelo Barraza-Alfaro[6], Myriam Benisty[7,8], Pietro Curone[9], Daniele Fasano[7,8], Cassandra Hall[10,11,12], Thomas Hilder[13], Andrés F. Izquierdo[5,14], Cristiano Longarini[15], François Ménard[16], Christophe Pinte[13,16], Jochen Stadler[7,17], Richard Teague[6], Jason Terry[18], David J. Wilner[4], Andrew J. Winter[19], Tomohiro C. Yoshida[20,21], and Brianna Zawadzki[22,23]

[1] Dipartimento di Fisica, Università degli Studi di Milano, Via Celoria 16, 20133 Milano, Italy; alessandro.ruzza@unimi.it
[2] Center for Computational Astrophysics, Flatiron Institute, USA
[3] Department of Physics and Astronomy, Stony Brook University, Stony Brook, NY 11794, USA
[4] Center for Astrophysics, Harvard & Smithsonian, Cambridge, MA 02138, USA
[5] Department of Astronomy, University of Florida, Gainesville, FL 32611, USA
[6] Department of Earth, Atmospheric, and Planetary Sciences, Massachusetts Institute of Technology, Cambridge, MA 02139, USA
[7] Université Côte d'Azur, Observatoire de la Côte d'Azur, CNRS, Laboratoire Lagrange, 06304 Nice, France
[8] Max-Planck Institute for Astronomy (MPIA), Königstuhl 17, 69117 Heidelberg, Germany
[9] Departamento de Astronomía, Universidad de Chile, Camino El Observatorio 1515, Las Condes, Santiago, Chile
[10] Department of Physics and Astronomy, The University of Georgia, Athens, GA 30602, USA
[11] Center for Simulational Physics, The University of Georgia, Athens, GA 30602, USA
[12] Institute for Artificial Intelligence, The University of Georgia, Athens, GA, 30602, USA
[13] School of Physics and Astronomy, Monash University, Clayton VIC 3800, Australia
[14] NASA Hubble Fellowship Program Sagan Fellow, USA
[15] Institute of Astronomy, University of Cambridge, Madingley Road, Cambridge CB3 0HA, UK
[16] University of Grenoble Alpes, CNRS, IPAG, B38000 Grenoble, France
[17] European Southern Observatory, Karl-Schwarzschild-Straße 2, D-85748 Garching bei München, Germany
[18] University of Oxford, Oxford, Oxfordshire, UK
[19] Astronomy Unit, School of Physics and Astronomy, Queen Mary University of London, London E1 4NS, UK
[20] National Astronomical Observatory of Japan, 2-21-1 Osawa, Mitaka, Tokyo 181-8588, Japan
[21] Department of Astronomical Science, The Graduate University for Advanced Studies, SOKENDAI, 2-21-1 Osawa, Mitaka, Tokyo 181-8588, Japan
[22] Department of Astronomy, Van Vleck Observatory, Wesleyan University, 96 Foss Hill Drive, Middletown, CT 06459, USA
[23] Department of Astronomy & Astrophysics, 525 Davey Laboratory, The Pennsylvania State University, University Park, PA 16802, USA
*Received 2025 November 17; revised 2026 January 10; accepted 2026 February 5; published 2026 March 16*

## Abstract

The exoALMA large program provided an unprecedented view of the morphologies and kinematics of 15 circumstellar disks, offering a biased but homogenous and well-characterized sample for population-level analysis. Continuum observations revealed numerous dust substructures, known to be potential signatures of embedded planets. We analyze the observed dust morphologies with the simulation-based inference tool DBNets2.0, assuming these are due to embedded planets at fixed locations, to infer the system's properties. We estimate the putative planet mass, the disk $\alpha$ viscosity, scale height, and dust Stokes number that would reproduce 19 substructures in 13 of the 15 exoALMA disks. We compare our results with literature estimates derived with different methods, and find good agreement in most cases. We further explore the implications of the inferred disk properties for accretion, showing that for the Herbig stars in our sample, the implied viscous accretion timescales are too long to account for their observed stellar accretion rates. Regarding planet migration, our results favor inward migration, with only three putative planets expected to migrate outward. Finally, we check for correlations of the inferred disk and planet properties with the disks' gas-to-dust mass ratio, nonaxisymmetry index, and masses of the gas, dust, and host stars, finding no remarkable trends.

*Unified Astronomy Thesaurus concepts:* Protoplanetary disks (1300); Astronomy image processing (2306); Astronomy data analysis (1858); Planetary system formation (1257)

## 1. Introduction

Substructures, such as gaps, rings, and cavities, are ubiquitous in protoplanetary and transition disk continuum observations (e.g., ALMA Partnership et al. 2015; A. Isella et al. 2016; S. M. Andrews et al. 2018; C. J. Clarke et al. 2018; G. Dipierro et al. 2018; S. E. van Terwisga et al. 2018; J. Huang et al. 2020; J. Bae et al. 2023; P. Curone et al. 2025). Although several mechanisms have been proposed to explain their origin (e.g., J. F. Hawley 2001; P. Barge et al. 2017; C. P. Dullemond & A. B. T. Penzlin 2018; X. Hu et al. 2019; J. Bae et al. 2023), planet–disk interaction remains one of the most promising and discussed (e.g., G. Dipierro et al. 2015; G. P. Rosotti et al. 2016; S. Zhang et al. 2018; G. Lodato et al. 2019; A. Ruzza et al. 2024, 2025) observationally confirmed in the two cases of PDS 70 (e.g., A. Isella et al. 2019; M. Keppler et al. 2019) and WISPIT 2 (R. F. v. Capelleveen et al. 2025). In this scenario, the observed dust substructures emerge due to gravitational interaction with embedded young planets, resulting in the formation of gaps and rings whose morphological

features depend on the physical properties of the system (K. D. Kanagawa et al. 2016, 2017; G. P. Rosotti et al. 2016; G. Dipierro & G. Laibe 2017; G. Lodato et al. 2019). Substructures can thus serve as an indirect probe for disk and planet properties that are still poorly constrained.

The large number of available observations enables gathering samples suitable for population-level statistically significant analysis and discussion, as done for instance in G. Lodato et al. (2019) and A. Ruzza et al. (2024, 2025). The estimation is done with simulation-based inference (SBI), which consists of fitting data with a model that is either the direct output of numerical simulations or a representation of that output. This process has been conducted manually by comparing synthetic observations to actual data (B. Veronesi et al. 2020; G. Dipierro et al. 2018; D. Fedele et al. 2018; S. Zhang et al. 2018; C. Toci et al. 2019) or through the calibration of empirical relationships (K. D. Kanagawa et al. 2016; R. Dong & J. Fung 2017; G. Lodato et al. 2019). A more recent alternative has been the use of machine learning techniques (S. Auddy & M.-K. Lin 2020; S. Auddy et al. 2021, 2022; S. Zhang et al. 2022; S. Mao et al. 2024; A. Ruzza et al. 2024, 2025; S. Shafaat Mahmud et al. 2026), which have shown significant advantages over other methods, combining the same speed and ease of use of empirical relations with the higher expressiveness of neural networks and the possibility, as done when fine-tuning simulations, of exploiting the entire observed morphology. These methods have demonstrated high accuracy on synthetic datasets and, in most cases, provided reliable quantification of the uncertainties.

The exoALMA Large Program (R. Teague et al. 2025) results represent a rare and valuable case of a homogenous sample of disk dust continuum observations. All of them present substructures in the millimeter continuum identified and characterized by P. Curone et al. (2025), with the sole exception of PDS 66. It should be noted, however, that substructures were also observed in this disk at higher resolution in similar wavelengths (Atacama Large Millimeter/submillimeter Array (ALMA) Band 7; A. Aguayo et al. 2025) and at longer (ALMA Band 3; A. Ribas et al. 2025), and shorter (S. G. Wolff et al. 2016) wavelengths, which trace different populations of dust grains. In this Letter, we aim to investigate what population of planets would be consistent with these substructures, assuming that each is the result of the disk interaction with an embedded young planet. We estimate, for all the objects in this sample, both the disks' and planets' physical properties. We then compare them with literature constraints and analyze their implications for both the observability and evolution of these systems.

To this end, we use DBNets2.0 (A. Ruzza et al. 2025, hereafter R25), a state-of-the-art SBI method that exploits machine learning techniques to enable a quick inference of the planet and disk properties that have a role in determining the observed morphology. Using neural posterior estimation (see, e.g., K. Cranmer et al. 2020), the full joint posterior for these properties is inferred, revealing degeneracies and enabling uncertainty quantification.

Further details regarding DBNets2.0 are provided in Section 2. Section 3 presents our motivation for the selection of this sample and our strategy for the analysis of each source. Results and systematic comparisons with previous studies are presented in Section 4 with further discussion in Section 5. In Section 6 we draw our conclusions.

## 2. DBNets2.0

DBNets2.0 is an SBI pipeline for rapidly fitting dust substructures, such as gaps, rings, and cavities, observed in disk dust continuum emission. Assuming the planet–disk interaction scenario, the tool takes as input the dust continuum observation, its angular resolution, and the assumed planet location, and infers the mass of the putative planet responsible for the observed substructures. In addition, it constrains three disk properties that can influence their morphology: the disk $\alpha$ viscosity (N. I. Shakura & R. A. Sunyaev 1973), gas aspect ratio ($h = H/R$), and dust Stokes number (St). To do that, DBNets2.0 uses convolutional neural networks (CNNs) and normalizing flows (see, e.g., G. Papamakarios et al. 2017), which allow inference of the full posterior distribution for the target properties, enabling an uncertainty-aware analysis and unveiling all existing degeneracies. The employed methods make the tool fast to apply to new data and easily scalable to larger datasets. Additionally, the extensive testing carried out in R25 on synthetic data demonstrated the accuracy of the inference results.

This pipeline is ultimately fitting data with a specific model, and all the inferred posteriors are to be understood as conditional upon it. This is not unique of SBI methods as the same is generally true for any technique of Bayesian inference with a model. In SBI, the model is implicitly defined by the training dataset, which, in this case, is composed of synthetic disk observations generated from the results of 2D hydrodynamical simulations. To clarify the assumptions underlying our results, we report in Appendix A the key steps and simplifications used to generate these data. Further details are provided in A. Ruzza et al. (2024, 2025). The inferred distributions cannot account for scenarios that are not included in this model. Therefore, it must be assessed if, or in which conditions, this model is appropriate to analyze the data. When the outlined assumptions can be made safely is, in general, an open question that goes beyond the scope of this work. We try to touch upon this issue first, more generally, in Appendix A and then in more detail by discussing, in Appendix B, each disk separately in light of all the information available from previous studies.

To support the analysis of whether the underlying model can reproduce the data, DBNets2.0 provides a metric called the "confidence score" (CS) that quantifies, with a value between zero and one, the similarity between the input continuum observation and the synthetic data within the DBNets2.0 training sample (the exact definition can be found in Appendix A). R25 identified 0.6 as a loose threshold between input data from the same distribution of the training dataset and random or out-of-distribution data. It was advised to treat with additional caution (or reject), any result with a CS less than this threshold. However, a small overlap around this threshold between in-distribution and out-of-distribution data was shown. Hence, in this work, since lower values are still close to this threshold, we adopt a conservative approach, considering estimates with CS $< 0.6$ as uncertain. We exclude these points from the presentation and discussion of aggregated results, but we still present them in plots where they can be clearly marked.

Additionally, because DBNets2.0, as any machine learning method, cannot safely extrapolate beyond the parameter space where it was trained, posteriors that extend beyond it should be regarded as nonconstraining. We identify as such all estimates

**Table 1**
Analyzed Disks, Putative Planet Locations, and Inferred Best Estimates of the Disk and Planet Properties

| Disk Name | $M_\star$ [$M_\odot$] | $R_p$ [au] | $R_{\rm edge}$ [au] | log $\alpha$ | $h$ | log St | $M_p$ [$M_{\rm Jup}$] | CS |
|---|---|---|---|---|---|---|---|---|
| AA Tau | 0.79 | 11 | ... | $-3.69^{+0.35}_{-0.39}$ | ... | ... | $2.22^{+2.17}_{-1.21}$ | 0.64 |
| | ... | 72 | ... | $-3.63^{+0.28}_{-0.23}$ | $0.07^{+0.00}_{-0.00}$ | $-1.51^{+0.12}_{-0.13}$ | $0.07^{+0.02}_{-0.02}$ | 0.84 |
| CQ Tau | 1.40 | 20 | 41 | $-3.71^{+0.49}_{-0.59}$ | $0.04^{+0.01}_{-0.01}$ | $-2.49^{+0.40}_{-0.36}$ | $2.34^{+0.93}_{-1.02}$ | 0.60 |
| DM Tau | 0.45 | 14 | ... | ... | ... | ... | ... | 0.66 |
| | ... | 72 | ... | $-2.26^{+0.20}_{-0.20}$ | $0.05^{+0.01}_{-0.01}$ | $-2.07^{+0.13}_{-0.12}$ | $0.05^{+0.02}_{-0.01}$ | 0.96 |
| *HD 135344B | 1.61 | 28 | 51 | $-2.78^{+0.29}_{-0.38}$ | $0.04^{+0.01}_{-0.01}$ | $-2.64^{+0.27}_{-0.34}$ | $2.46^{+0.74}_{-0.68}$ | 0.49 |
| | ... | 66 | ... | $-3.82^{+0.20}_{-0.18}$ | $0.07^{+0.01}_{-0.01}$ | $-1.56^{+0.13}_{-0.14}$ | $0.23^{+0.07}_{-0.06}$ | 0.68 |
| HD 143006 | 1.56 | 22 | ... | ... | $0.07^{+0.04}_{-0.01}$ | $-2.76^{+0.37}_{-0.41}$ | $2.59^{+1.41}_{-1.36}$ | 0.73 |
| | ... | 52 | ... | $-3.40^{+0.33}_{-0.28}$ | $0.08^{+0.01}_{-0.01}$ | $-1.28^{+0.22}_{-0.23}$ | $0.33^{+0.14}_{-0.09}$ | 0.63 |
| HD 34282 | 1.61 | 47 | 124 | $-3.72^{+0.20}_{-0.18}$ | $0.07^{+0.02}_{-0.02}$ | $-1.89^{+0.36}_{-0.35}$ | $7.14^{+3.33}_{-1.76}$ | 0.67 |
| J1604 | 1.29 | 41 | 82 | $-2.99^{+0.31}_{-0.31}$ | $0.06^{+0.01}_{-0.01}$ | $-2.05^{+0.37}_{-0.36}$ | $7.91^{+1.52}_{-1.37}$ | 0.86 |
| J1615 | 1.14 | 83 | ... | $-2.35^{+0.19}_{-0.17}$ | $0.07^{+0.01}_{-0.01}$ | $-2.46^{+0.19}_{-0.20}$ | $0.29^{+0.08}_{-0.07}$ | 0.95 |
| J1852 | 1.03 | 31 | ... | $-2.38^{+0.22}_{-0.27}$ | $0.07^{+0.01}_{-0.01}$ | $-1.82^{+0.22}_{-0.28}$ | $2.12^{+0.72}_{-0.66}$ | 0.61 |
| *LkCa 15 | 1.14 | 42 | 68 | $-2.93^{+0.17}_{-0.16}$ | $0.08^{+0.01}_{-0.01}$ | $-2.52^{+0.19}_{-0.17}$ | $1.63^{+0.28}_{-0.26}$ | 0.54 |
| | ... | 86 | ... | $-3.76^{+0.25}_{-0.22}$ | $0.06^{+0.00}_{-0.00}$ | $-1.45^{+0.12}_{-0.14}$ | $0.07^{+0.02}_{-0.02}$ | 0.72 |
| *MWC 758 | 1.40 | 30 | ... | $-3.55^{+0.31}_{-0.37}$ | $0.04^{+0.01}_{-0.01}$ | $-2.23^{+0.30}_{-0.32}$ | $2.35^{+0.57}_{-0.43}$ | 0.52 |
| SY Cha | 0.77 | 33 | ... | $-3.78^{+0.17}_{-0.17}$ | $0.07^{+0.02}_{-0.01}$ | $-1.81^{+0.34}_{-0.34}$ | $2.47^{+0.82}_{-0.63}$ | 0.61 |
| V4046 Sgr | 1.73 | 8 | ... | $-3.75^{+0.34}_{-0.38}$ | ... | ... | $3.73^{+3.25}_{-1.96}$ | 0.86 |
| | | 20 | ... | $-3.32^{+0.18}_{-0.17}$ | $0.09^{+0.01}_{-0.01}$ | $-2.83^{+0.17}_{-0.17}$ | $1.49^{+0.36}_{-0.28}$ | 0.67 |

**Note.** Putative planet locations within cavities are underlined. In these cases, we also report the cavity edge ($R_{\rm edge}$), which we reference in Section 5.2. CS quantifies, with a value between zero and one, the similarity of the input observation to DBNets2.0 training data. Following R25, CS $\leqslant 0.6$ indicates poor representation of the respective dust morphology in the DBNets2.0 training data. Therefore, they must be treated with additional caution and uncertainty. We mark these cases with an asterisk before the disk name. Because lower CS values are still close to this threshold, we still provide all our results. Unconstrained estimates are not reported in the table.

whose 2.5th and 97.5th percentiles (corresponding to $2\sigma$ for a Gaussian) fall outside of the respective prior support. As for estimates with CS $< 0.6$, unconstrained estimates are removed from our presentation and discussion of aggregated results, while they are marked as uncertain in plots that distinguish individual estimates.

## 3. Sample Selection and Methodology

For this study, we considered all fiducial Band 7 continuum observations of the exoALMA Large Program, which were CLEANed, calibrated, and made publicly available by the exoALMA collaboration (P. Curone et al. 2025; R. A. Loomis et al. 2025; R. Teague et al. 2025). It is important to note that the exoALMA sample is inherently affected by selection biases, leading to an overrepresentation of brighter and more extended disks (for details see R. Teague et al. 2025).

DBNets2.0 requires as input a proposed planet location to fit the observed substructures. In this Letter, we separately consider each disk and propose the locations of embedded planets based on all available information, including dust morphology and relevant literature. Table 1 presents a summary of the proposed planet locations derived from this discussion, while Appendix B outlines the considerations that guided these choices.

As a general strategy, we consider as viable planet locations those of gaps and cavities identified by P. Curone et al. (2025) through the characterization of the azimuthally symmetric `frank` (J. Jennings et al. 2020) fits of the disks' continuum emission. We also follow P. Curone et al. (2025)'s characterization when distinguishing between gaps and cavities. We note that both types of substructures are equally represented in the DBNets2.0 training dataset (see A. Ruzza et al. 2024, 2025). In addition to the P. Curone et al. (2025) selection criteria, we exclude substructures that are not visible in the azimuthally averaged radial profiles obtained from the CLEANed images, such as the D63 gap in J1842, and consider shallow gaps in low signal-to-noise ratio observations only if a planet at the same location was already proposed in previous studies.

In some disks with multiple gaps, we assume multiple planet locations, interpreting the results as described in Appendix A. In the case of cavities, planets could be located over a wider range of radii, and the DBNets2.0 output is sensitive to this choice (see Section 5.2). We select the putative planet's location based on previous studies that proposed detections of planet signatures such as direct thermal emission or kinematic perturbations, and exclude from our main discussions the cavity of J1842, which lacks such constraints. However, because these detections remain debated, in Appendix C we provide DBNets2.0 estimates as a function of the assumed planet location, including J1842 in this analysis.

For each disk and putative planet, the output is an estimate of the posterior distribution $p(\alpha, h, {\rm St}, M_p/M_\star|x, \mathcal{M})$ conditioned on observation $x$ and underlying model $\mathcal{M}$ discussed in Section 2. All analyses and results presented here are based on $10^6$ samples drawn from each inferred posterior distribution. The conversion from $M_p/M_\star$ to $M_p$ is done using dynamical stellar masses derived by A. F. Izquierdo et al. (2025).

## 4. Results and Comparison with the Literature

Individual results for each proposed planet are reported in Table 1 and Appendix D. We also report the CSs of DBNets2.0 estimates, which, in three cases, fall below the rejection threshold (CS $= 0.6$) set by R25. These are three

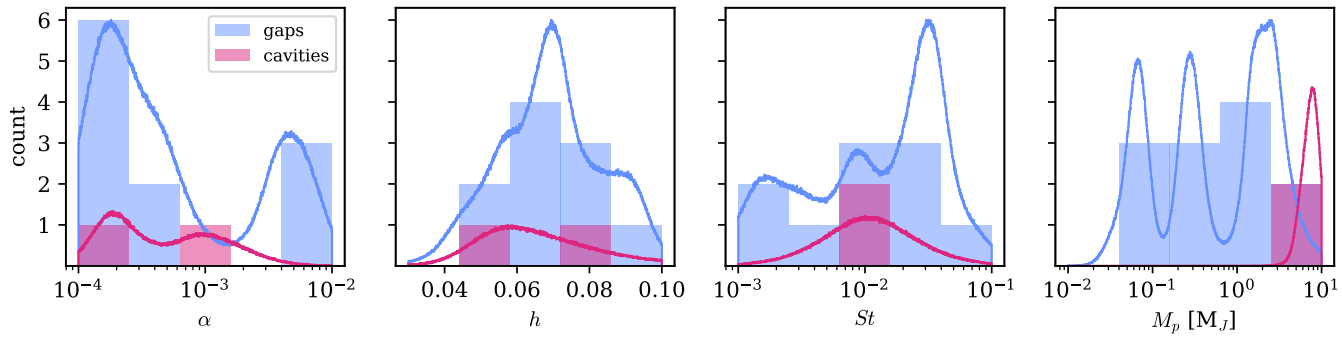


**Figure 1.** Distributions of the four inferred properties for the full sample, excluding results considered uncertain or unconstrained. The shaded histograms show the medians of the individual posterior distributions, while the overlaid curves represent the stacked posteriors, normalized for comparison. *y*-axis ticks refer to the histograms. Contributions from putative planets located in gaps (blue) and in cavities (pink) are shown separately.

estimates for putative planets in the inner gap of MWC 758 and in the cavities of HD 135344 B and LkCa 15. Additionally, unconstrained estimates are removed from Table 1 and marked in red in Appendix D. They mainly occur for substructures at small radial distances from the host star. In the rest of the Letter, following the approach already mentioned in Section 3, unconstrained estimates and those with CS $< 0.6$ are removed from our presentation and discussion of aggregated results, while they are marked as uncertain in plots that distinguish individual estimates.

Figure 1 shows the distributions of the four inferred properties for the full sample, excluding uncertain estimates. No noteworthy trends are evident in the distributions of $h$ and St. The inferred $\alpha$-viscosity distribution presents two peaks at the two ends of the DBNets2.0 prior (see Appendix A.3), with a higher number of sources showing evidence of low viscosity, in line with the results found on the larger sample analyzed in R25 and with several literature studies (e.g., K. M. Flaherty et al. 2015; R. Teague et al. 2016; S. Zhang et al. 2018; G. P. Rosotti 2023). Among the three systems with high viscosity estimates is the noteworthy case of DM Tau, further discussed in Section 4.2, where there is evidence of a high level of turbulence (S. Guilloteau et al. 2012; K. Flaherty et al. 2020). We checked but did not observe any common characteristics distinguishing the high- and low-viscosity groups that could account for the observed bimodality.

In contrast to R25, where 83% of planets had masses below $1\,M_{\rm Jup}$, in this case the distribution of planet masses extends significantly to higher values. This result may reflect the exoALMA target-selection strategy, which favored the most massive disks, arguably more likely to host massive observable companions. The three-peak distribution is due to the combination of the low number and high precision of our mass estimates. Cavities are found to suggest the presence of more massive companions ($\geqslant 1\,M_{\rm Jup}$) while no clear distinction is observed for the other disk properties. It should be noted that for cavities, after removal of those unconstrained or uncertain, only two estimates are shown for each property, although they do not all correspond to the same two putative planets. The details of which estimates are shown, with precise values, can be found in Table 1.

### 4.1. Planet Masses

For most of the analyzed dust substructures, previous works suggested the presence of possibly embedded planets as reviewed in Appendix B. Many of these studies put constraints on the masses of proposed planets using several approaches. Figure 2 presents a comparison of our planet-mass estimates with the literature.

Nondetections in HCI and SAM observations are translated into upper limits on the planet masses. These are computed assuming different models for the planet emission and therefore depend on them and on the underlying assumptions (M. Willson et al. 2016; M. Reggiani et al. 2018; T. Currie et al. 2019; T. Uyama et al. 2020; R. Asensio-Torres et al. 2021; J. de Boer et al. 2021; T. Stolker et al. 2024; N. L. Wallack et al. 2024; F. Maio et al. 2025). We report in Figure 2 the most constraining upper limits estimated assuming the warmer planet models, which would thus predict higher fluxes. We do not report the less constraining limits as those would, in all cases, be well above the upper end of our planet-mass prior ($10^{-2}\,M_\star$). We found our estimates to be mostly consistent with these constraints, with the only two exceptions of J1604 and LkCa 15, for which we estimate higher planet masses. However, results might be reconciled with colder models for the planet's emission (C. Mordasini et al. 2012) or extinction from the disk material (e.g., F. Alarcón et al. 2024). In the case of LkCa 15 specifically, literature studies observed significant gas emission within the cavity and argued this would be best explained by collective interaction with multiple planets (M. Leemker et al. 2022; C. H. Gardner et al. 2025), a situation that would be outside DBNets2.0's scope, as it was trained on examples of planet–disk interaction with only one planet.

For HD 135344 B and MWC 758, tentative detections of point-source-like emission allowed F. Maio et al. (2025) and M. Reggiani et al. (2018) to also put lower limits on the planet masses. Nevertheless, as stated in F. Maio et al. (2025), the presence of a circumplanetary disk (CPD) around the putative planet might loosen these constraints. Interestingly, the three mass estimates for the putative planets in LkCa 15 (for $R_p = 42$ au), HD 135344 B, and MWC 758 have a CS lower than the advised rejection threshold. Furthermore, all these cases, including J1604, are cavities, and thus the DBNets2.0 estimates can vary depending on the assumed planet position. This issue is discussed in detail in Section 5.2, illustrated with the case of J1604.

Planet masses estimated using empirical relations (e.g., R. Dong & J. Fung 2017) with gap widths and depths and fine-tuned numerical simulations tend to agree, within the uncertainties, with DBNets2.0 results. Although J1604 and the cavity of LkCa 15 still represent notable exceptions.

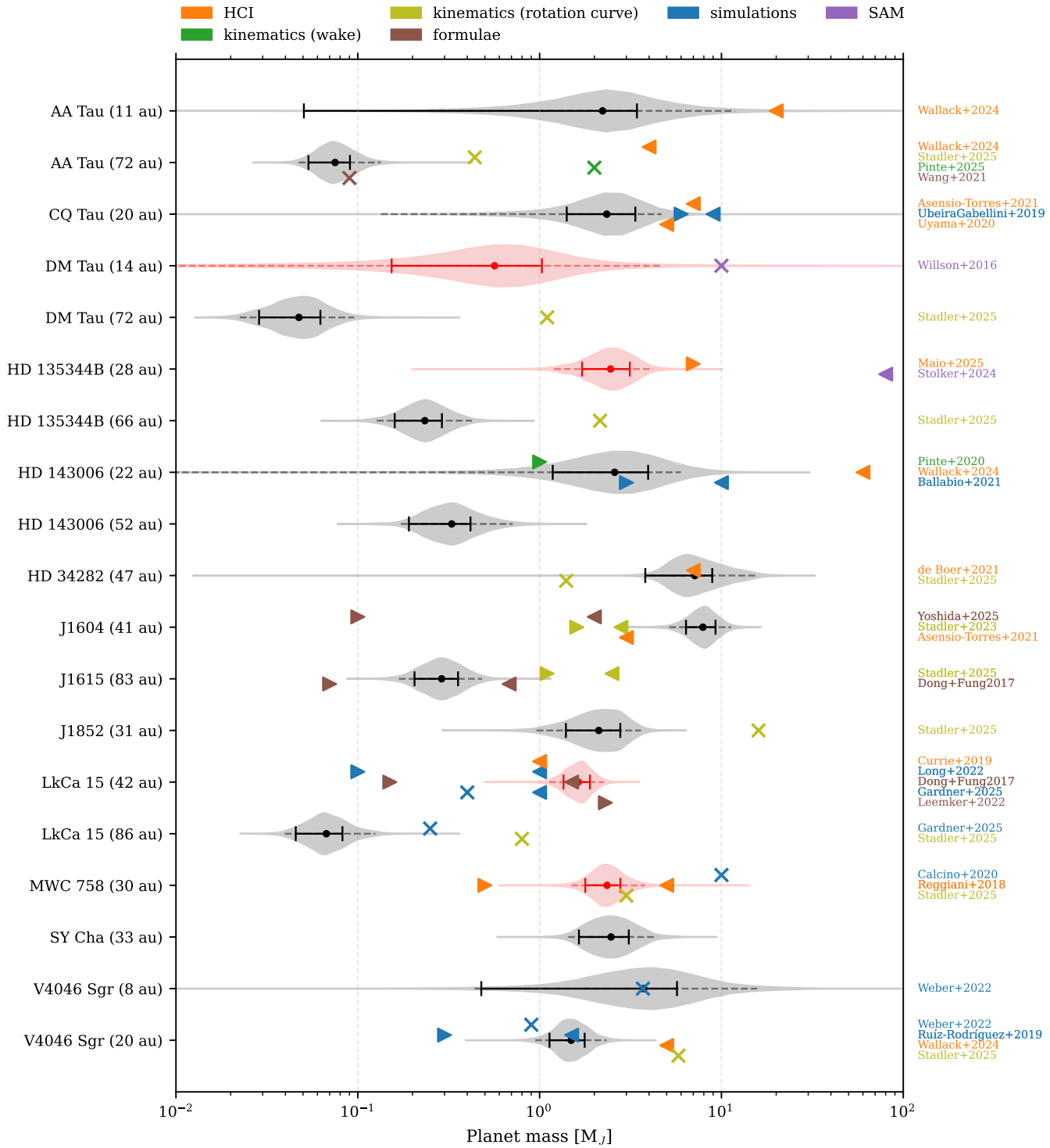


**Figure 2.** Overview of all inferred posterior distributions for the mass of the proposed planets (gray and red violins) and comparison with constraints provided in previous studies. The continuous error bars mark the 16th, 50th, and 84th percentiles of the respective distribution, while the dashed lines go from the 2.5th to the 97.5th percentiles. Red violins mark uncertain estimates. Right and left facing arrows mark, respectively, lower and upper limits, while crosses indicate estimates. Different colors are used to distinguish between the methods used to provide these constraints: high-contrast imaging (HCI); sparse aperture masking (SAM); empirical relationships with gap width and depth ("formula"); numerical modeling of dust observations ("simulations"); estimates from localized kinematic perturbations in channel maps, tracing the planet wake ("kinematics (wake)"); and estimates from gas pressure dips observed through rotation curves ("kinematics (rotation curves)"). Full references can be found throughout Section 4.1 and Appendix B.

Across our sample of proposed planet locations, only two of them match that of a proposed kinematic signature in the disks' channel maps, discussed in C. Pinte et al. (2025) for AA Tau, and in C. Pinte et al. (2020) for HD 143006. All other kinematic perturbations proposed by C. Pinte et al. (2025) as planet signatures are located outside the extent of the observed continuum. In the case of HD 143006, only a lower limit on the planet's mass was provided by C. Pinte et al. (2020), based on the observability of the target planet. This is consistent with our mass estimate. In the case of AA Tau, through a

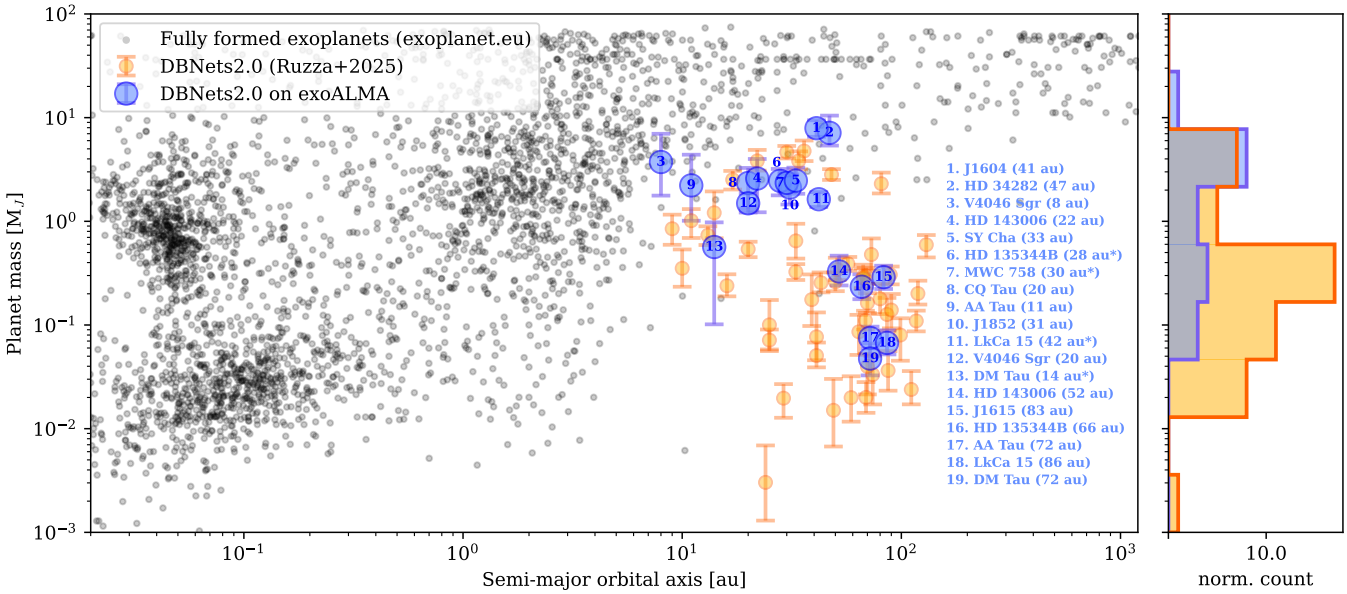


**Figure 3.** Inferred planet masses as a function of the putative planet's radial location. Blue points and histogram bins mark DBNets2.0 planet-mass estimates for the exoALMA sample presented in this Letter. Respective disk names and assumed planet locations are listed in descending order according to the inferred planet mass. Asterisks mark uncertain or unconstrained estimates. Orange points and histogram's bins mark DBNets2.0 estimates for the larger sample of substructured disks considered in R25. Black points mark all confirmed exoplanets; data are from exoplanet.eu/home/.

comparison with synthetic data, the authors provided a planet-mass estimate, which is significantly overestimated relative to our value. Interestingly, this seems common for mass estimates from kinematic signatures as discussed, for example, in C. Pinte et al. (2020) and V. Elbakyan et al. (2022). With the two exceptions of HD 34282 and J1604, for which previous caveats apply, we observe the same systematic overestimation as the J. Stadler et al. (2023, 2025) estimates. These works provided the masses of planets potentially driving observed perturbations in the gas azimuthal velocity (rotation curves) interpreted as gas pressure dips. The planet masses were inferred using the empirical relation proposed by H. Gyeol Yun et al. (2019), which links planet mass to the radial width of the perturbed region. This relation was shown to exhibit weak dependence on the disk $\alpha$ viscosity.

Figure 3 shows the masses of the proposed planets inferred using DBNets2.0 as a function of their putative location. It is remarkable how proposed planets in dust substructures populate a region of this parameter space that was otherwise inaccessible with standard exoplanet detection techniques, and suggests the possibility of different planetary system architectures. On the other hand, this planet population would also be significantly younger, raising the question of how it would evolve with time. Furthermore, looking at individual sources in this plot is particularly relevant for selecting suitable targets for direct imaging of the planet's thermal emission, which is easier to observe in the case of massive planets far from the host star. According to these criteria, our analysis suggests HD 34282 and J1604 as the most promising candidates. This remains true even including the substructured disks analyzed in R25. We should note, though, that this result refers to putative planets in the specific locations indicated in Table 1 and informed by previous studies. As discussed in Section 5.2, these results could change if the planet orbits were different. In the right panel of the same figure we show that proposed planets in the substructures of the exoALMA disk sample are typically more massive than those emerging from the larger sample of dust substructures analyzed in R25.

### 4.2. Turbulent Viscosity

As mentioned in Section 4, the distribution of $\alpha$ viscosity for the entire sample is skewed toward the lower end of the DBNets2.0 prior. DM Tau is one of the few cases for which there are robust measures of line broadening interpreted as a high level of turbulence (S. Guilloteau et al. 2012; K. Flaherty et al. 2020) corresponding to $\alpha = 0.08 \pm 0.02$. Similarly, C. Hardiman et al. (2026) performed a full radiative transfer modeling of $^{12}$CO $J = 3$–2 and CS $J = 7$–6 finding that data are best fit by nonthermal line broadening corresponding to $\alpha = 0.16^{+0.01}_{-0.02}$. It must be noted that our training of DBNets2.0 with synthetic data with $\alpha$ values up to $10^{-2}$ effectively sets a prior on the returned estimates, preventing the inference of higher values. Nevertheless, the DBNets2.0 fit of dust substructures in this disk yields a picture consistent with that in the presented literature.

For the gap at 14 au $\alpha$ is not constrained by our analysis, probably due to low spatial resolution, as the obtained posterior extends over the entire support of the prior. The analysis of the gap at 72 au instead returns an estimate $\alpha = 5.5^{+3.1}_{-2.0} \times 10^{-3}$, skewed toward higher values than the other disks. Although this is not directly compatible with the mentioned literature estimates, several caveats apply. First, as already mentioned, the DBNets2.0 priors are too constraining in this case; second, line-broadening measures refer to the localized regions where the molecular emission is detected, which are both at larger radii and well above the midplane, whereas our estimate is sensitive to the turbulence near the midplane at the substructure radial location. The modeling indeed indicates that, depending on the mechanism, velocity perturbations could increase with height (see, e.g., J. B. Simon et al. 2015, for turbulence driven by magneto-rotational instability).

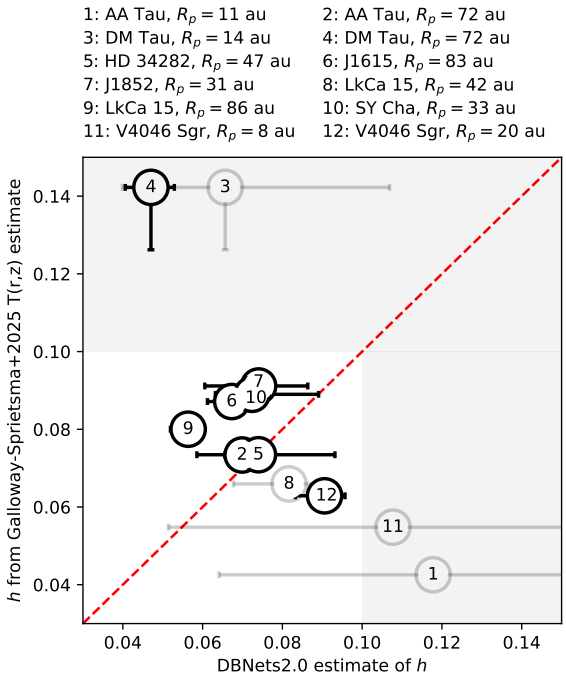


**Figure 4.** Comparison between the aspect-ratio estimates obtained with DBNets2.0 and the temperature-profile measurements reported by M. Galloway-Sprietsma et al. (2025). For this comparison, the midplane temperatures are converted into disk aspect ratios under the assumptions of vertical hydrostatic equilibrium and a vertically isothermal structure, consistent with the physical model used to train DBNets2.0. Faded points indicate sources with unreliable or unconstrained estimates. The red dashed line denotes perfect agreement between the two methods. The gray background marks parameter values that fall outside of DBNets2.0's scope.

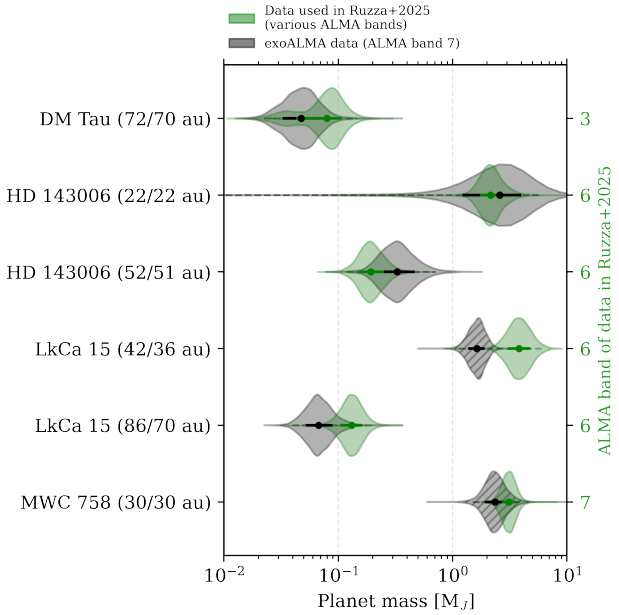


**Figure 5.** Comparison, for the overlapping objects, of DBNets2.0 estimates derived in R25 on archival data (green violins) with those obtained in this work on the exoALMA observations (black violins). On the right, in green, the band of the continuum observation used in R25 is shown. Near each disk name we report the assumed planet locations, respectively in R25 and in this work. Violin plots of estimates corresponding to CSs below the acceptance threshold in either work are hatched.

### 4.3. Aspect Ratios and Stokes Numbers

Via line profile analysis of exoALMA observations, M. Galloway-Sprietsma et al. (2025) located the emission surfaces of observed emission lines, deriving the thermal structures of some exoALMA disks. These temperatures, extrapolated to the disks' midplanes, can be compared to our estimates of the disks' aspect ratios by converting them under the assumption of vertical hydrostatic equilibrium. Figure 4 presents this comparison done by using the M. Galloway-Sprietsma et al. (2025) estimates of the midplane temperature profile to compute the expected aspect ratio at the putative planet locations where the DBNets2.0 estimates are given. We observe no correlation between the two estimates, although M. Galloway-Sprietsma et al. (2025) typically found higher temperatures. The same was observed and discussed in M. Galloway-Sprietsma et al. (2025) comparing their temperature estimates with those derived from the disks' scale heights and simulations, suggesting the need for an improved temperature-profile prescription. Although in some cases the M. Galloway-Sprietsma et al. (2025) temperatures imply disk aspect ratios higher than those in DBNets' prior, we note (see Figure 1) that our estimates do not saturate toward the prior's upper limit.

Regarding Stokes number estimates, we highlight the case of LkCa 15. For this disk, A. Sierra et al. (2025) performed a multiwavelength analysis of the observed rings, deriving, through a comparison with dust trapping models, a plausible range of dust Stokes numbers for each of the three rings at 42, 69, and 101 au. However, these also depend on the chosen model for the opacity. With DBNets2.0, we were only able to constrain St close to the gap at 86 au. In this case, we estimate $\log \mathrm{St} = -1.45^{+0.12}_{-0.14}$. This is in line with A. Sierra et al. (2025)'s estimates for the two outer rings, $-1.17 < \log \mathrm{St} < 0.36$, which assume DSHARP opacities (T. Birnstiel et al. 2018). Using the L. Ricci et al. (2010) opacities instead yielded the wider range $-2.46 < \log \mathrm{St} < 0.81$, which covers almost entirely the DBNets2.0 prior (see Appendix A.3).

## 5. Discussion

### 5.1. Comparison with DBNets2.0 Estimates in A. Ruzza et al. (2025)

In Figure 5 we compare, for the overlapping sample, the DBNets2.0-inferred planet masses for the exoALMA Band 7 ($\lambda = 0.8$–$1.1$ mm) data with those presented in R25 for the same objects but obtained from the analysis of different observations, in most cases taken at different wavelengths (Band 6: $\lambda = 1.1$–$1.4$ mm and Band 3: $\lambda = 2.6$–$3.6$ mm). Interestingly, the estimates are compatible within the uncertainties, proving little dependence of these results on the band of the observations. We separately highlight the case of MWC 758 for which we are comparing the analysis of observations at the same wavelength but with different resolutions. Specifically, the observation used in R25 is better resolved by a factor of 2, which translates to a compatible but more precise estimate than that obtained on the exoALMA data. The same is also observed across different wavelengths for the case of HD 143006, for which the observation used in R25 is resolved approximately 2.7 times better.

This general agreement is also observed for the other inferred properties, as shown in Figure 14 of Appendix E. The largest difference emerges for the inferred $\alpha$ viscosity in

DM Tau, for which the DBNets2.0 analysis of a longer-wavelength (Band 3) observation results in a lower value by more than 1 order of magnitude. Roughly speaking, a continuum observation mainly traces dust grains of size $a = \lambda/2\pi$, where $\lambda$ is the observed wavelength. Therefore, since $St \propto a$, a change $\Delta\lambda/\lambda$ should correspond to the same relative change $\Delta$St in the Stokes number of the observed dust grains. This relative difference is ∼30% for Bands 6 and 7 and ∼60% for Bands 7 and 3. R25 demonstrated that DBNets2.0 typically achieves a 10% precision on the Stokes number estimates and thus should be sensitive to a change in observational wavelength. This, however, is not observed in practice, probably because the effect of St on the ring and gap morphology is degenerate with $\alpha$. We already noted this in R25, where we interpreted it as indicating that the inference is primarily driven by morphological features associated with dust trapping and diffusion (e.g., ring prominence). Hence, DBNets2.0 may be interpreting the differences in dust substructures as due instead to a different $\alpha$ viscosity, which indeed varies the most when comparing Band 3 and 7 observations. Furthermore, the fact that DBNets2.0 was trained on synthetic observations generated at Band 6 wavelengths might play a role. From this analysis, we conclude that we should not fully trust the DBNets2.0 estimates on $\alpha$ and St when those are inferred using observations at wavelengths significantly different than those of Band 6. Our tests instead show that using Band 7 observations yields compatible results within the given uncertainties.

### 5.2. Dependence of DBNets2.0 Estimates on the Assumed Planet Location

We explained in Section 2 that the radial location of the planets proposed in disk substructures must be provided as one of DBNets2.0's inputs. This is needed to rescale the observation and match the physical scale of the training dataset.

The inference results can easily change with different assumptions on the planet location as a natural consequence of the change, after rescaling, of the measures of the substructures' morphological features, such as gap and ring widths, as well as their distance to the planet. This ambiguity is not particularly relevant for the analysis of gaps, as the alleged planet location can be easily constrained, for example, by assuming the intensity minimum in the azimuthally averaged radial profile. For cavities, instead, the situation is more delicate as there is often no indication of plausible planet locations and the range of possible positions is typically wide. Figure 6 illustrates this degeneracy for the inferred planet-mass estimates in the specific case of the J1604 cavity terminating with a bright ring at 80 au. As expected, the inferred planet mass decreases as the assumed planet location approaches the ring.

The same is expected for all other planets assumed within disk cavities. For this reason, in those cases, we only included in our sample planet the locations previously suggested by independent methods and observations. We present plots similar to Figure 6 for the other inferred disk properties in Appendix C along with the same analysis performed for all the cavities in our sample. We define the cavity radius identifying $R_{\rm edge}$ as the peak of the ring outside the cavity. In general, the estimated planet mass appears independent of the assumed

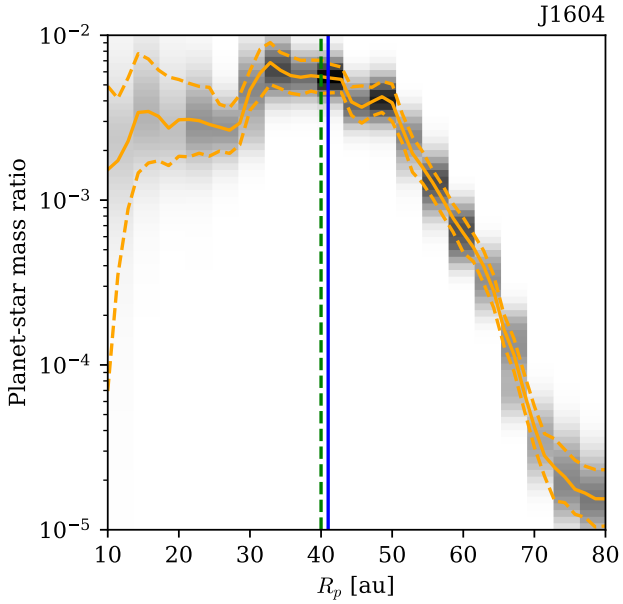


**Figure 6.** Degeneracy of the DBNets2.0 planet-mass estimate with the assumed planet radial location in the cavity of the J1604 disk. The overlaid orange lines mark the 16th, 50th, and 84th percentiles of the inferred distribution. The vertical blue line marks the location of the putative planet assumed in this study. The vertical green dashed line indicates $R_{\rm edge}/2$, where $R_{\rm edge}$ is the radial location of the peak of the ring outside the cavity.

radial location as long as it lies within one-half of the cavity radius (green dashed line in Figures 10 and 11 in Appendix C), while it decreases progressively as the planet approaches the outside ring. As shown in the same figure, estimates for the other disk properties are also affected by the choice of the planet position, although their dependence on it is less intuitive.

### 5.3. Accretion Timescales

Assuming a self-similar density profile, C. Longarini et al. (2025) modeled the rotation curves of a subsample of exoALMA targets, fitting the stellar mass, disk mass, and scale radius with the method introduced in G. Lodato et al. (2022). The same analysis was also performed on the MAPS (K. I. Öberg et al. 2021) disks sample in P. Martire et al. (2024). Combining these results with literature measures of the stars' accretion rates, C. Longarini et al. (2025) constrained the disk accretion timescales, assuming the self-similar solution to the disk evolution, as (L. Hartmann et al. 2016)

$$(t_{\rm acc}/t_{\rm dyn})^{-1} \sim \alpha h^2 = \frac{2}{3}\frac{\dot{M}}{M_{\rm disk}\,\Omega_c}, \tag{1}$$

where $t_{\rm dyn} = \Omega^{-1}$ and $\Omega_c$ is the Keplerian velocity at the disk scale radius. This relation captures the global accretion flow and, as cautioned by C. Longarini et al. (2025), the derived $\alpha$ (or $\alpha h^2$) must be interpreted as an estimate of the disk accretion regardless of the mechanism that drives it. Conversely, with DBNets2.0, we can provide local estimates of $\alpha h^2$ obtained by modeling substructures due to planet–disk interaction, whose formation and morphology are sensitive to the value of the viscosity (or turbulence).

In the scatterplots of Figure 7 we compare the estimates of the two methods for the exoALMA disks for which dynamical masses have been measured (C. Longarini et al. 2025). We

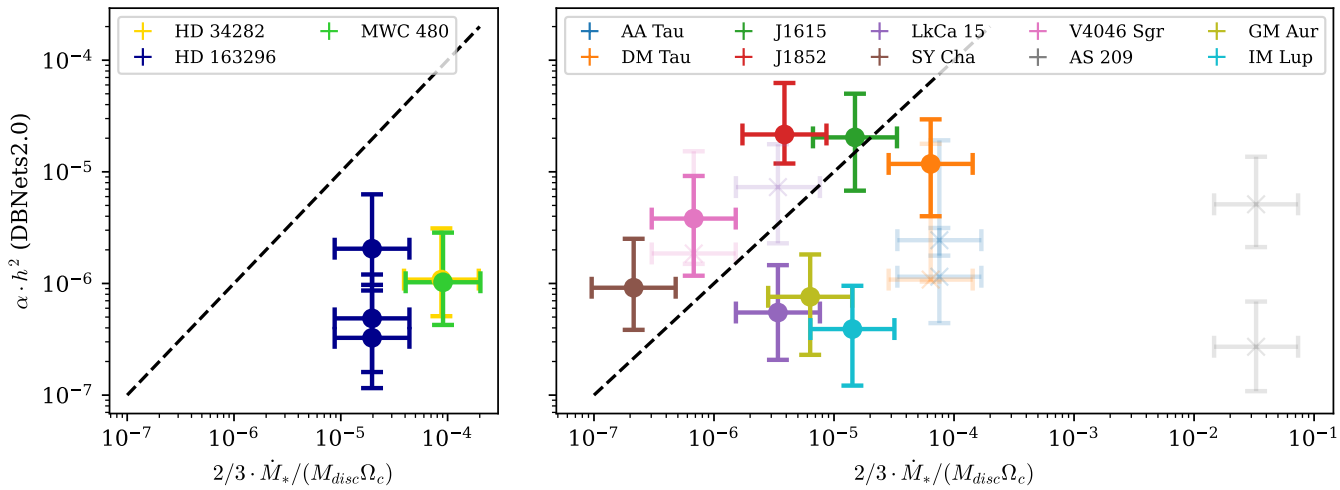


**Figure 7.** Comparison of DBNets2.0's local estimates of viscous-accretion timescales with the global accretion rates derived from measurements of star accretion (J.-F. Donati et al. 2011; J. R. Fairlamb et al. 2015; C. F. Manara et al. 2023) and disk masses (P. Martire et al. 2024; C. Longarini et al. 2025). The left panel presents the comparison for all Herbig stars in the sample, while the right panel refers to T Tauri stars. Faded points mark unreliable or unconstrained estimates of $\alpha h^2$ or $M_{\rm disk}$. The dashed black lines mark the equality between the quantities on the two axes.

combine in the same plot the same estimates for MAPS disks, obtained using P. Martire et al. (2024)'s disk dynamical masses and R25's DBNets2.0 estimates for $\alpha$ and $h$. The left panel presents these results for Herbig stars in the considered sample, while T Tauri stars are shown in the right panel. Interestingly, we observe that for all Herbig stars in our sample, our measure of the disk timescale for viscous transport cannot explain the observed accretion rate, suggesting that additional accretion mechanisms should be invoked to reproduce the observed timescales. The results obtained for T Tauri stars present instead a larger scatter, although in most cases the two estimates are roughly consistent, implying that the magnitude of viscous transport inferred from planet–disk interaction signatures could alone explain the measured accretion rates. Note that we marked with fading colors all points for which one of the two estimates is considered uncertain or unconstrained. DBNets2.0's overestimation of $\alpha h^2$ for some disks may be due to their substructured nature, which would alleviate the validity of the self-similar hypothesis and, therefore, of Equation (1). Indeed, some studies suggested that the presence of planets could reduce mass accretion into the host star (e.g., W. A. Müller Tobias & W. Kley 2013; C. F. Manara et al. 2019; C. Bergez-Casalou et al. 2020).

### 5.4. Kanagawa Coefficients and Stalling Radius

The effects and physics of planet–disk interaction and their dependence on the system's properties are often summarized into two parameters $K$ and $K'$ defined as

$$K' = \left(\frac{M_p}{M_\star}\right)^2 \alpha^{-1} h^{-3}, \tag{2}$$

$$K = \left(\frac{M_p}{M_\star}\right)^2 \alpha^{-1} h^{-5}. \tag{3}$$

For example, K. D. Kanagawa et al. (2015) have found that the depths of the gas gaps carved by planets scale approximately as $1/(1 + 0.04K)$, while K. D. Kanagawa et al. (2016) showed that the gap width scales as $\Delta_{\rm gap} \propto K'^{1/4}$. In Figure 8 we show the $K$ and $K'$ computed for each proposed planet using DBNets2.0's estimates of the disk and planet properties.

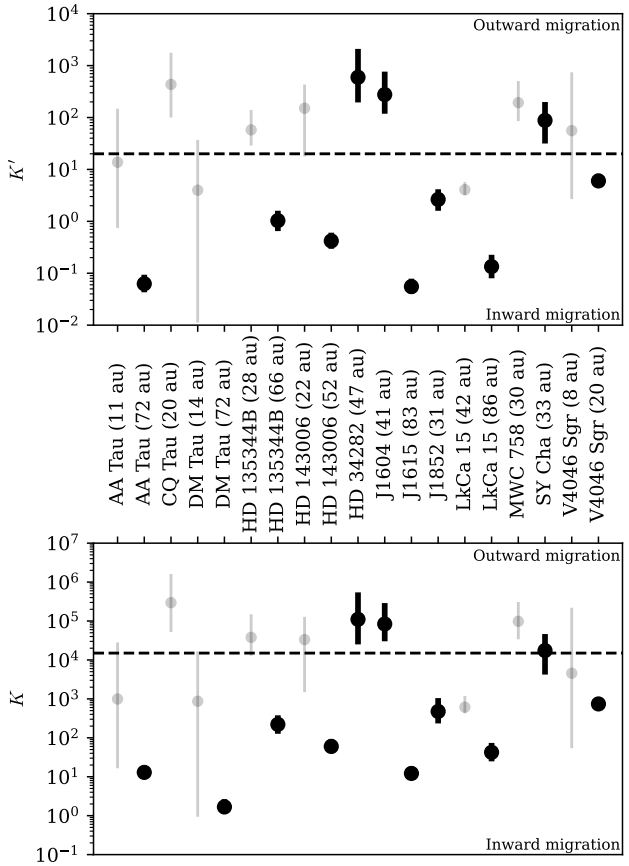


**Figure 8.** The $K'$ (upper panel) and $K$ (lower panel) coefficients, defined in Equations (2) and (3), respectively, derived for all analyzed disks from DBNets2.0 estimates. The horizontal dashed lines mark the threshold values of $K' = 20$ and $K = 1.5 \cdot 10^4$ for the expected direction of planet migration. Faded points indicate sources with unreliable or unconstrained estimates.

An interesting application of these parameters regards the phenomenon of planet migration, for which numerical modeling (A. M. Dempsey et al. 2021; C. E. Scardoni et al.

2022) has shown $K$ and $K'$ values to control its direction (inward or outward). Specifically, as their values increase, at the thresholds $K = 1.5 \cdot 10^4$ and $K' = 20$, the planet would switch from inward to outward migration. The values shown in Figure 8 indicate that, excluding points with unconstrained or uncertain estimates and independently of assuming migration to be determined by $K$ or $K'$, most of our planets would fall into the inward migrating case, with only three objects migrating outwards.

Typically, as the disk aspect ratio is expected to increase further from the star, both $K$ and $K'$ would decrease at increasing radii, thus an initially outward migrating planet would at some point switch to inward migration. Following this reasoning C. E. Scardoni et al. (2022) proposed the existence of a stalling radius, which would correspond to the locations where $K$ and $K'$ equal the threshold values controlling the migration sign. The high scatter in the $K$ and $K'$ inferred values indicates that we do not observe an accumulation of planets in proximity of the expected stalling radii.

It is important to note that the model used to analyze dust substructures, implicitly defined by the simulations used to train the DBNets2.0 algorithm, does not include planet migration, as planets are held on a fixed orbit. Therefore, the effects of this phenomenon on the dust morphology (F. Meru et al. 2019; P. Nazari et al. 2019) are not considered.

### 5.5. Configurations of Proposed Multiple Systems

For six disks in the sample, we propose the presence of two planets. We thus question first whether the proposed planet locations correspond to specific resonances and, second, the stability of these three-body systems. We check the latter according to the Hill criterion proposed by B. Gladman et al. (1993), which poses a threshold on the mutual distance of the two planets $d$ in terms of their mutual Hill radius $R_H = [(m_1 + m_2)/3M_\star]^{1/3}[(a_1 + a_2)/2]$. This is required to be greater than $2\sqrt{3}$ for the system to be stable. Results are presented in Figure 9 where, for each one of the six proposed multiple systems, the $x$-axis indicates the mutual distance of the two planets over their mutual Hill radius $d/R_H$ while the $y$-axis is the ratio between their Keplerian velocities. According to this analysis, all these systems would be dynamically stable and are not close enough to lie in the lower-order mean-motion resonances (MMRs; such as 3:2 or 2:1).

### 5.6. Correlations with Other Disk Properties

We explored any possible relation between DBNets2.0's best estimates for $\alpha$, $h$, St, and $M_p$ and disk properties measured from the exoALMA data. Specifically, we considered the disk gas-to-dust mass ratios, nonaxisymmetry index (NAI) quantifying the axisymmetry of continuum observations, the disk dynamical masses, the disk dust masses, and the host star masses (P. Curone et al. 2025; A. F. Izquierdo et al. 2025; C. Longarini et al. 2025). We do not observe any statistically significant correlation, with the sole exception of the pair stellar mass–aspect ratio, which is detailed in the right panel of Figure 15 in Appendix F. This likely arises because more massive stars have higher luminosity, and thus their stronger irradiation is reflected in the disk temperature. Details and results of this analysis are presented in Appendix F.

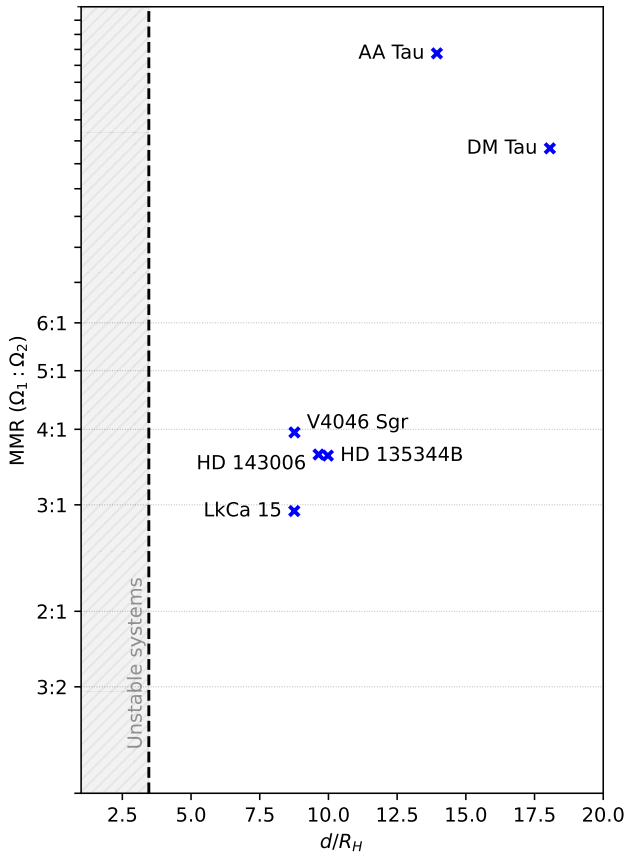


**Figure 9.** Disks where we assumed two fiducial planet locations. The $x$-axis shows the mutual distance of the two planets in the proposed three-body systems with respect to their mutual Hill radius. The vertical dashed line marks the stability threshold $d/R_H = 2\sqrt{3}$ found by B. Gladman et al. (1993). According to their criterion, the orbits of planets whose mutual distance is lower are unstable. The $y$-axis indicates the ratio between the keplerian angular velocities at the two planet locations. Ticks on the $y$-axis indicate MMRs.

## 6. Conclusion

In this Letter, we examine the dust substructures revealed by exoALMA continuum observations, interpreting them as signatures of planet–disk interaction to characterize the properties of possible embedded planets and their host disks. For this purpose, we employed the SBI pipeline DBNets2.0 (R25), which exploits deep learning methods to quickly and accurately perform a statistical inference of the disk $\alpha$ viscosity, scale height, dust Stokes number, and planet mass. The inference of full posterior distributions allowed for proper uncertainty quantification, and the application of two criteria made it possible to flag and separate uncertain estimates, ensuring the robustness of the overall results.

Carefully inspecting each observation and reviewing previous studies we propose a population of 19 planets possibly embedded in 13 of the 15 disks targeted by the exoALMA program. After applying DBNets2.0 to each one of these putative planets we discuss the results, their comparison with previous works, and their implications. The main outcomes of this study are the following.

1. We identify dust substructures in the exoALMA disk sample that might most promisingly host young planets. We provide mass estimates for these putative planets and discuss them in the context of the current literature. Most of our estimates are consistent with upper limits set by

high-contrast imaging and estimates from simulations or empirical formulae. Putative planets in the cavities of J1604 and LkCa 15 are expected to be more massive than what constrained by previous estimates. However, the estimate for LkCa 15 is associated with a low confidence score and, in both cases, these estimates depend on the assumed planet location. Specifically, a lower mass would be consistent with the planet being further from the star.

2. Due to their separation from the host star and inferred high mass, we find the proposed planets in HD 34282 and J1604 to be the most suitable for attempting direct imaging observations.
3. Most of the proposed planets are super-Jovian, likely due to sample selection bias.
4. Cavities require larger planet masses than gaps.
5. Interpreting the observed substructures as due to planet–disk interaction, we provide estimates of three disk properties: $\alpha$ viscosity, disk scale height, and dust Stokes number. For DM Tau our analysis interestingly suggests a high value of the $\alpha$ viscosity, in agreement with constraints from line-broadening measures (S. Guilloteau et al. 2012; K. Flaherty et al. 2020).
6. Derived estimates of the disks' viscous timescales ($\alpha h^2$) are too long to explain the measured accretion rates of Herbig stars, while they present a trend consistent with most measures of accretion rates and disk masses in T Tauri stars.
7. Derived parameters controlling the migration direction indicate the regime of inward migration to be more frequent, although three putative planets would undergo outward migration.
8. We find a statistically significant correlation between the stellar masses and inferred disks' aspect ratios (Pearson correlation coefficient of 0.60). We do not observe any other correlation of the inferred quantities with other disk properties.

In addition to these results, the analysis demonstrates the effectiveness of SBI tools, and in particular DBNets2.0, for performing quick and systematic studies of large observational surveys. Homogeneous samples of disk and planet properties, affected by the same model, observational assumptions, and systematics, can help address fundamental questions of planet formation and evolution, as demonstrated in this work. While not all dust substructures may originate from planet–disk interactions, if a substantial fraction do, then systematic analyses of large samples can still provide meaningful insights into the population-level properties of young planets, especially when combined with complementary observations and methods. Single results can additionally explain the outcomes of direct imaging surveys and lead future observations toward the most promising candidates.

## Acknowledgments

This Letter makes use of the following ALMA data: ADS/JAO.ALMA#2021.1.01123.L. ALMA is a partnership of ESO (representing its member states), NSF (USA) and NINS (Japan), together with NRC (Canada), MOST and ASIAA (Taiwan), and KASI (Republic of Korea), in cooperation with the Republic of Chile. The Joint ALMA Observatory is operated by ESO, AUI/NRAO, and NAOJ. The National Radio Astronomy Observatory is a facility of the National Science Foundation operated under cooperative agreement by Associated Universities, Inc.

G.R. acknowledges support from the Fondazione Cariplo, grant no. 2022-1217 and from the European Research Council (ERC) under grant agreement No. 101039651 (DiscEvol). G.L. acknowledges support from PRIN-MUR 20228JPA3A, from the European Union Next Generation EU, CUP: G53D23000870006. G.L. and A.R. acknowledge support from the European Union's Horizon Europe Research & Innovation Programme under the Marie Sklodowska-Curie grant agreement No. 823823 (DUSTBUSTERS). S.F. is funded by the European Union (ERC, UNVEIL, 101076613) and acknowledges financial contribution from PRIN-MUR 2022YP5ACE. J.B. acknowledges support from NASA XRP grant No. 80NSSC23K1312. M.B., J.S., and D.F. have received funding from the European Research Council (ERC) under the European Union's Horizon 2020 research and innovation program (PROTOPLANETS, grant agreement No. 101002188). P.C. acknowledges support by the ANID BASAL project FB210003. C.H. acknowledges support from NSF AAG grant No. A. T.H. is supported by an Australian Government Research Training Program (RTP) Scholarship. Support for A.F.I. was provided by NASA through NASA Hubble Fellowship grant No. HST-HF2-51532.001-A awarded by the Space Telescope Science Institute, which is operated by the Association of Universities for Research in Astronomy, Inc., for NASA, under contract NAS5-26555. C.L. has received funding from the UK Science and Technology research Council (STFC) via the consolidated grant ST/W000997/1. C.P. acknowledges Australian Research Council funding via FT170100040, DP18010423, DP220103767, and DP240103290. A.J.W. has been supported by the Royal Society through a University Research Fellowship, grant No. URF\R1\241791. T.C.Y. acknowledges support by grant-in-aid for JSPS Fellows JP23KJ1008. Support for B.Z. was provided by the Brinson Foundation. F.M. has received funding from the European Research Council (ERC) under the European Union's Horizon Europe research and innovation program (grant agreement No. 101053020, project Dust2Planets). Views and opinions expressed by ERC-funded scientists are, however, those of the author(s) only and do not necessarily reflect those of the European Union or the European Research Council. Neither the European Union nor the granting authority can be held responsible for them.

## Appendix A
## Details of DBNets2.0 and Underlying Assumptions

As specified in Section 2, DBNets2.0, as any other SBI model, is ultimately fitting the input data with a model that is defined by its training dataset. This consists of synthetic protoplanetary disk observations of the dust continuum emission with planet-induced substructures. To generate these synthetic observations, we first ran hydrodynamical simulations and then postprocessed their results. In this appendix, we provide details on this procedure and on additional aspects of DBNets2.0. We highlight the main underlying assumptions and briefly discuss their implications for interpreting the results. Further details can be found in R25.

### A.1. Details on the Hydrodynamical Simulations

Hydrodynamical simulations are run with the mesh code FARGO3D (P. Benitez-Llambay & F. S. Masset 2016; see J. Bae et al. 2025, for a systematic comparison between hydrodynamical codes). One, nonaccreting planet is embedded in the disk and maintained on a fixed orbit. We adopt a locally isothermal equation of state with a set temperature profile. The disk evolves viscously with viscosity parameterized through the N. I. Shakura & R. A. Sunyaev (1973) prescription with constant $\alpha$ across the entire simulation domain; this effective viscosity is used to model the effects of turbulence. Dust is modeled as a pressureless fluid subject to diffusion, with Schmidt number $Sc = 1$, and gas drag with fixed Stokes number across the entire simulation domain. Back reaction of the dust on the gas is neglected.

### A.2. Radiative Transfer and Additional Postprocessing of Synthetic Observations

Using the simulated disks' dust density ($\Sigma_d$) and temperature ($T_d$), synthetic observations are generated by computing the surface brightness as $T_s = T_d(1 - e^{\kappa\Sigma_d})$, which is the radiative transfer solution for a vertically homogenous (in temperature and dust properties), face-on disk. The opacity ($\kappa$) is computed using the T. Birnstiel et al. (2018) model. We note that other machine learning–based methods (e.g., S. Shafaat Mahmud et al. 2026) exist that rely on radiative transfer calculations. In our setup (based on 2D simulations with a prescribed temperature structure and a single-sized dust grain population) the primary advantage of radiative transfer methods is their ability to properly account for disk inclination, which causes photons to traverse longer paths spanning a range of disk radii. We expect this effect to introduce significant differences only for highly inclined disks, which is not the case for the sample considered here. During training, Gaussian noise with random variance is added, and the images are convolved with Gaussian beams of varying sizes to ensure that the results are robust to these observational effects.

### A.3. Training Set Parameter Space: Effectively Setting the Inference Priors

The training set covers the parameter space region where $10^{-4} \leqslant \alpha \leqslant 10^{-2}$, $0.03 \leqslant h \leqslant 0.1$, $10^{-3} \leqslant \mathrm{St} \leqslant 10^{-1}$, and $10^{-5} \leqslant M_p/M_\star \leqslant 10^{-2}$. This effectively sets uniform priors for each of these inferred properties in the respective range of values. Two additional parameters, $\sigma$ and $\beta$, are varied, within our training dataset. These are the slopes of the power laws that set the initial radial profile of, respectively, the disk surface density and aspect ratio. The value of $\beta$ is uniformly sampled in the range $0 \leqslant \beta \leqslant 0.35$ while $\sigma$ is set to match the steady state solution as $\sigma = 2\beta + 1/2$, therefore spanning the range $0.5 \leqslant \sigma \leqslant 1.2$. DBNets2.0's inferred posteriors are marginalized with these priors over these parameters.

### A.4. Definition of the Confidence Score

The CS, introduced in Section 2, given observation $x$ and DBNets2.0 estimate $p(\theta|x)$, is computed as follows: (1) we sample 10 $\theta_i$ from $p(\theta|x)$, (2) we linearly interpolate the synthetic images in the training dataset at all $\theta_i$, (3) we remap the interpolated images $b_i$ and the input image $x$ to polar coordinates, (4) we compute the fast Fourier transform of the remapped $b_i$ and $x$, (5) we compute CS as

$$\mathrm{CS} = 1 - \frac{1}{10}\sum_i \frac{(|F(x)| - |F(b_i)|)^2}{(|F(x)|^2 + |F(b_i)|^2)}. \tag{A1}$$

### A.5. Deprojection and Preprocessing of Input Observations

Observations need to be deprojected before being input into DBNets2.0. We do that by linearly interpolating the observation and using the geometrical properties fitted by P. Curone et al. (2025). In A. Ruzza et al. (2024) we proved, for synthetic data, that the results remain unaffected by deprojection effects up to a disk inclination of 60°. The result should also hold for R25, as both build on the same CNN to process the data. All disks in the exoALMA sample satisfy this criterion. We note that the CS is computed using the input image after deprojection. Therefore, possible artifacts introduced by the deprojection could, in principle, lead to a reduction in CS, although this has not been tested.

Input observations are also standardized by subtracting the mean value of their pixels and dividing by their standard deviation (see R25).

### A.6. Treatment of Multiple Substructures

For the analysis of disks with multiple substructures, we separately consider each gap as a viable planet location and independently fit our single-planet model. Each DBNets2.0 output considers, in principle, the entire observed morphology within $0.3R_p$ and $4R_p$, corresponding to the portion of the disk provided as input. The parameter $R_p$, representing the putative planet's radial location, is required as an additional input to rescale the observation to the training convention ($R_p = 1$), thereby ensuring consistency between the input image and the data used to train the model. No additional preprocessing or masking of secondary gaps is performed.

The more conservative approach would thus be to consider each result as an independent scenario where the disk has only one embedded planet at the specified location, producing all substructures within this disk region. However, although a systematic test is still pending, we can reasonably assume that the inferred posteriors are mainly informed by the closest substructures to the planet location, as was demonstrated with a similar CNN model by S. Zhang et al. (2022). If this were true, our estimates would still be valid for a system with multiple planets, given that the effect of their mutual interaction on the disk morphology can be neglected. We only use this assumption in Figure 9 to speculate about the configuration of these potentially multiple systems. We also note that S. Shafaat Mahmud et al. (2026) developed an autoencoder-based pipeline (called VADER) to estimate planet masses from dust substructures in protoplanetary disks, trained on synthetic observations containing up to three planets. In their study, they compared the mean planet-mass predictions from VADER and DBNets (A. Ruzza et al. 2024) for multiplanet and single-planet systems and found no statistically significant difference between the two groups.

## Appendix B
## Details of Sample Selection and Relevant Literature

In the following we discuss, for each source, our choices for the proposed planet locations reviewing the continuum radial profiles published in P. Curone et al. (2025) and relevant literature.

### B.1. AA Tau

This disk exhibits three pairs of gaps and rings in the `frank` radial profile, along with one fainter outer pair. Both R. A. Loomis et al. (2017) and P. Curone et al. (2025) present evidence suggesting a misalignment of the inner disk. We propose D11 (11 au) as the first location for a putative planet. The two gap–ring pairs D64–B72 and D80–B90 correspond to only one gap in the CLEAN data. Notably, C. Pinte et al. (2025) proposed a kink detection at this location (B72), although with a low (∼5) signal-to-noise ratio. Other studies, such as S. Wang et al. (2021), have considered this substructure as a unique planet-hosting gap. Therefore, we assume 72 au, coincident with the ring in the `frank` profile, as our fiducial location for a second putative planet. The outer gap–ring substructure is too faint for our analysis.

### B.2. CQ Tau

This disk presents a cavity-like morphology and spiral-like nonaxisymmetric features consistent with the prominent spirals observed in SPHERE scattered-light images by I. Hammond et al. (2022). An inner companion is proposed as responsible for inducing such spirals. P. Curone et al. (2025) also revealed a faint inner disk. M. G. Ubeira Gabellini et al. (2019) modeled this disk with hydrodynamical and radiative transfer simulations finding that a planet with a minimum mass of 6 to 9 $M_{\rm Jup}$, located at 20 au from the star, could qualitatively reproduce the observed dust morphology. We assume 20 au as our proposed location for a putative planet.

### B.3. DM Tau

This disk presents an inner gap at 14 au, which we propose as the first location for a putative planet. M. Willson et al. (2016) found a potential point source at ∼6 au through sparse aperture masking interferometry, consistent with a planet of roughly 10 $M_{\rm Jup}$. Two pairs of gap–ring substructures further from the central star are also observed. We assume these to be due to a single planet at 72 au, consistent with other studies (T. Uyama et al. 2017; S. Wang et al. 2021; L. Francis et al. 2022). K. Flaherty et al. (2020)'s line-broadening measures yielded results compatible with high levels of turbulence.

### B.4. HD 135344 B

This disk exhibits a central cavity ending with a bright ring at 51 au, which might be eccentric. A second ring with a prominent azimuthal asymmetry is located at 78 au. The asymmetry can be explained with a vortex that might alone explain the disk morphology (P. Cazzoletti et al. 2018). IR observations reveal a prominent spiral structure (e.g., T. Muto et al. 2012; A. Garufi et al. 2013; T. Stolker et al. 2016). We propose two putative planets. One inside the cavity at 28 au, consistent with the location of the point-like feature observed by F. Maio et al. (2025). The second planet is proposed inside the gap at 66 au. B. Veronesi et al. (2019)'s numerical modeling of the spiral structure observed in scattered light suggests that it may be due to two embedded planets. Additionally, the observation of a change in the pitch angle of the IR spiral and a filament in the continuum data, first observed by S. Casassus et al. (2021) and confirmed by P. Curone et al. (2025), further supports the presence of the outer companion.

### B.5. HD 143006

This is a well-studied source also present in the DSHARP (S. M. Andrews et al. 2018) survey. The continuum observations show two gaps located at 22 and 52 au, which we assume as possible locations for embedded planets. C. Pinte et al. (2020, 2025) claim the detection of a possible planetary signature in the disk kinematics approximately at the location of the inner gap. G. Ballabio et al. (2021) with hydrodynamical simulations suggested a 3–10 $M_{\rm Jup}$ planet located at 32 au within the dust gap observed in scattered light.

### B.6. HD 34282

This disk presents a central cavity and several faint outer gap–ring pairs, which are only clearly distinguishable in the `frank` profile. J. de Boer et al. (2021) observed a single arm spiral in IR, which would be better explained by a low-mass planet inside its location. Outer gaps are too faint to apply DBNets2.0, therefore, we only assume the presence of one planet at 47 au corresponding to a shoulder in the depleted inner cavity, as revealed by the `frank` radial intensity profile.

### B.7. J1604

This source exhibits a large cavity depleted both in gas and dust. A bright ring is located at 82 au. Kinematical analysis provides evidence for a warp and reveal non-Keplerian features, including a spiral-like structure with a small (6°–14°) pitch angle (J. Stadler et al. 2023; C. Pinte et al. 2025). J. Stadler et al. (2023) found these features to be consistent with a planet located at 42 au, which we thus also assume as a tentative planet location. T. C. Yoshida et al. (2025) modeled this disk's surface density finding a drops by a factor of ∼2–2.5 at ∼60 au. Using K. D. Kanagawa et al. (2015)'s formula and the measured gap depth they estimated a putative planet mass between 0.1 and 2 $M_{\rm Jup}$.

### B.8. J1615

This disk presents three pairs of faint gaps and rings, two of which are too faint to sustain a DBNets2.0 analysis. We consider as a putative planet location the remaining gap at 83 au. C. Pinte et al. (2025) propose the detection of a planet kinematical signature located outside the region of continuum emission.

### B.9. J1842

J1842 has an internal cavity with shadows that suggest the presence of an unseen inner ring. There are no proposed detections of planet signatures within this cavity that could inform us on a plausible planet location, and DBNets2.0's results would be too dependent on the location choice. A gap at 63 au is revealed by the `frank` fit but is too faint to yield reliable results. C. Pinte et al. (2025) propose a planet at $r_p = 105$ au, which is outside the region of continuum emission. We thus remove this disk from our sample of fiducial planets, but we still provide results for different planet locations in Appendix C.

### B.10. J1852

J1852 shows an internal cavity with a faint ring at 19 au, which was previously proposed by M. Villenave et al. (2019).

The location of maximum depletion within the cavity, i.e., 31 au, is proposed as a possible planet location.

### B.11. LkCa 15

This disk presents one cavity and one gap. Several studies focused on this source exploring different scenarios for planetary companions. We consider two fiducial planet locations. The first would be at 42 au consistent with literature claims and likely responsible for the B68 ring. The second planet would be in the gap at 86 au. F. Long et al. (2022) claimed that the observed substructures, including asymmetric features, are best reproduced with more than one planet. M. Leemker et al. (2022) observationally constrained the gas surface density across the cavity. They found evident gas depletion inside 10 au, which they suggested might be due to a Jovian planet, whereas they observed high gas density in the dust-depleted region between 10 and 68 au, which was interpreted as a result of a chain of low-mass planets. C. H. Gardner et al. (2025) modeled both continuum and gas observations using hydrodynamical and radiative transfer simulations, enforcing M. Leemker et al. (2022)'s hypothesis for the cavity and concluding that other plausible scenarios for the entire morphology could be either other processes that do not involve planets or three planets at 29, 51, and 80 au with masses of 3–5 $M_{\rm Jup}$, 0.4 $M_{\rm Jup}$, and 0.25 $M_{\rm Jup}$, respectively. C. Pinte et al. (2025) proposed detections of planet kinematic signatures, which, however, lie outside of the continuum emission region.

### B.12. MWC 758

This disk presents a central cavity with a small inner disk and strong asymmetries that have been attributed to the global spiral structure clearly visible in scattered-light observations (C. A. Grady et al. 2013; M. Benisty et al. 2015). The spiral origin is disputed, but several studies argued for a planetary perturber in the outer disk (B. Ren et al. 2018, 2020) with a tentative detection through HCI by K. Wagner et al. (2019). However, B. Ren et al. (2018) and J. Calcino et al. (2020) suggested that an eccentric perturber inside the cavity would also be possible. A point-like emission south of the star at a deprojected separation of 20 au was detected by M. Reggiani et al. (2018) who suggested a CPD around a low-mass companion between 0.5 and 5 $M_{\rm Jup}$ as the more likely explanation. For this object, we use DBNets2.0 following the second hypothesis and therefore assuming a planet inside the cavity at 30 au at the location of the minimum in the `frank`-fitted radial profile emission.

### B.13. SY Cha

This is a transition disk with a dust morphology that resembles that of PDS 70 while being less gas depleted in the inner cavity or gap. The presence of an inner disk with an extension of a few astronomical units makes this a prototype disk for the formation of a solar-system-like planetary system. Both R. Orihara et al. (2023) and P. Curone et al. (2025) reported observations of nonaxisymmetric features in the dust continuum. We found no previous studies suggesting putative planets inside the gap. For our analysis, we assume a planet companion at a radial location of 33 au, corresponding to the gap minimum.

### B.14. V4046 Sgr

This is a tight binary whose disk exhibits two concentric gaps with an inner disk that is off-center with respect to the outer disk. This may be explained by a misalignment of the inner binary, which could also account for the rest of the dust substructures (H. Aly & G. Lodato 2020). However, the planetary origin has also been explored. D. Ruíz-Rodríguez et al. (2019) focused on the outer gap, checking its morphology against a set of hydrodynamical (and radiative transfer) simulations, concluding that the most likely explanation would be a Jovian planet. P. Weber et al. (2022) also considered an inner gap, successfully reproducing dust substructures in simulations with two embedded planets of 3.7 $M_{\rm Jup}$ and 0.9 $M_{\rm Jup}$ at 9 and 20 au, respectively. Therefore, for our analysis we consider two fiducial planets at 8 and 20 au. However, caution is advised in this case as, if both planets were present, their small separation would more likely result in the substructures' morphology being affected by the presence of the second companion, a situation that is outside the scope of our tool.

## Appendix C
## Degeneracy with the Planet Location within Cavities

We illustrate in Figures 10 and 11 how DBNets2.0's estimates for the disk properties $M_p$, $\alpha$, $h$, and St vary as the planet is assumed in different positions inside the observed substructures. The variation of the DBNets2.0 CS is also reported in the same figures. Figure 10 presents the results of this analysis for all disk cavities where we assumed the presence of embedded planets. Figure 11 presents three additional cases for which is worth performing this analysis, namely J1852, MWC 758, and J1842. In the two former cases, putative planets are located within large gaps with an inner boundary defined, respectively, by a small inner disk and by a faint ring. These peculiar morphologies make the putative locations of embedded planets uncertain. The latter disk, instead, presents an inner cavity but was excluded from our sample due to the lack of other works or evidence suggesting a possible planet location.

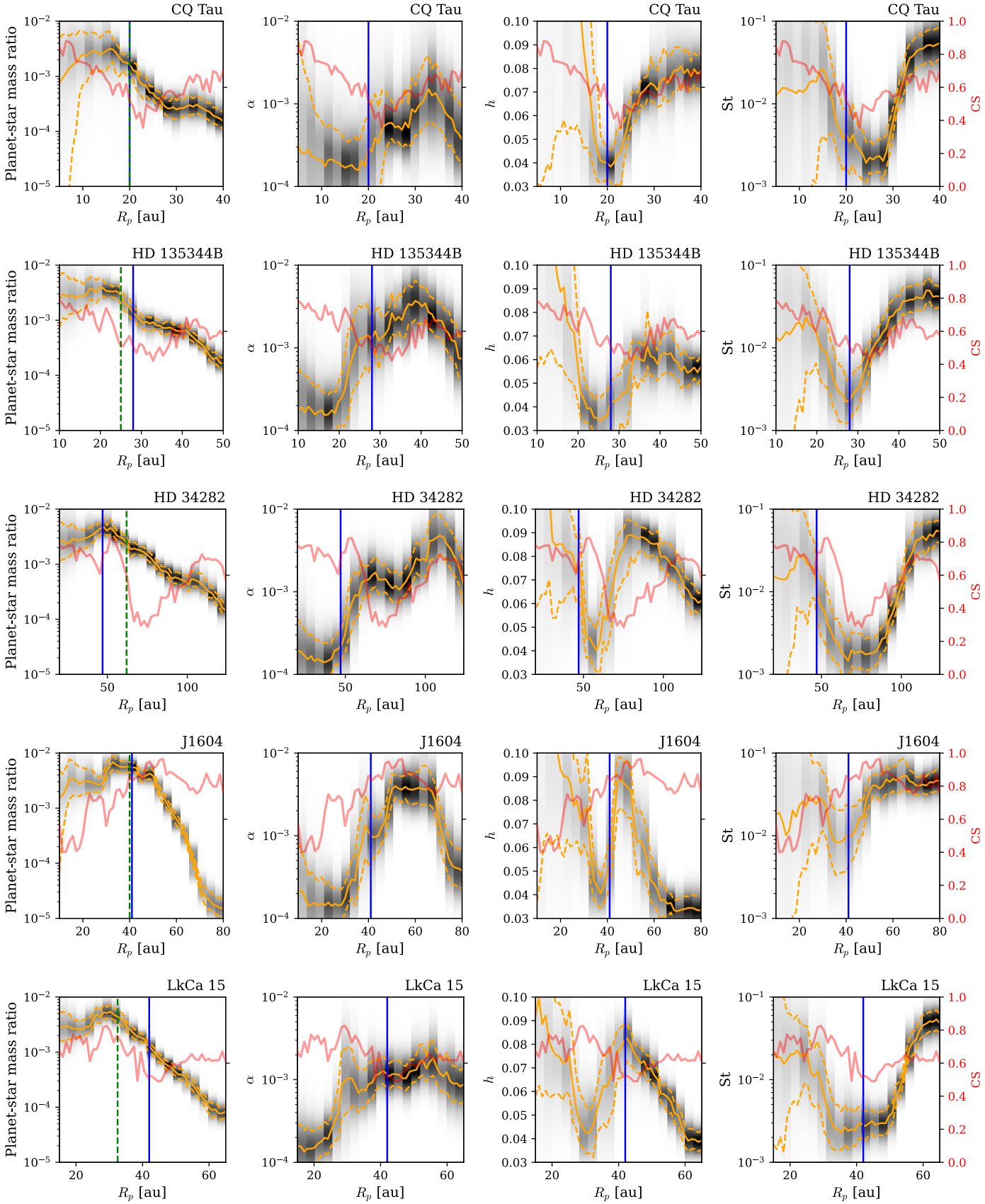


**Figure 10.** Sensitivity of DBNets2.0-inferred disk properties to the assumed planet location for all cavities considered in this study. The black 2D histograms represent the inferred distributions. The overlaid orange lines mark the 16th, 50th, and 84th percentiles of the inferred posterior distributions. The vertical blue lines indicate the fiducial planet locations assumed in this work. The vertical green dashed lines mark $R_{\rm edge}/2$, where $R_{\rm edge}$ is the radial location of the cavity edge. The red lines indicate the DBNets2.0 CS.

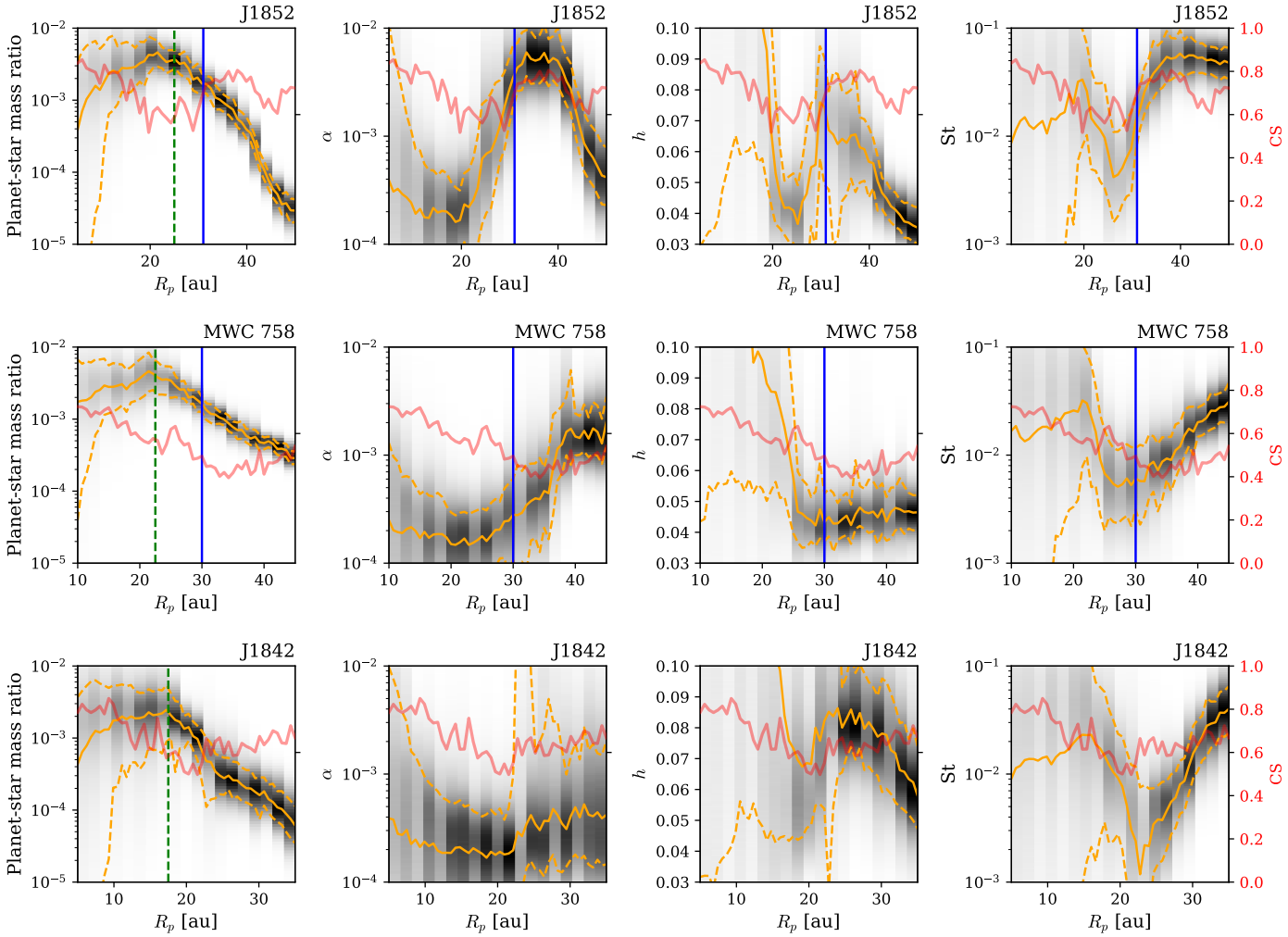


**Figure 11.** Sensitivity of DBNets2.0-inferred disk properties to the assumed planet location for the three peculiar cases of J1852, MWC 758, and J1842. In the two former disks, the considered substructures are large gaps with, respectively, a small inner disk and a faint inner ring. The latter disk presents a cavity, which was discarded from our analysis due to the lack of previous works suggesting possible planet locations. The black 2D histograms represent the inferred distributions. The overlaid orange lines mark the 16th, 50th, and 84th percentiles of the inferred posterior distributions. The vertical blue lines indicate the putative planet locations assumed in this work. The vertical green dashed lines mark $R_{\rm edge}/2$, where $R_{\rm edge}$ is the radial location of the cavity edge. The red lines indicate the DBNets2.0 CS.

## Appendix D
## All Individual Results

Figures 12 and 13 present singularly all the results of the application of DBNets2.0 to the selected targets. Best estimates with uncertainties are also listed in Table 1.

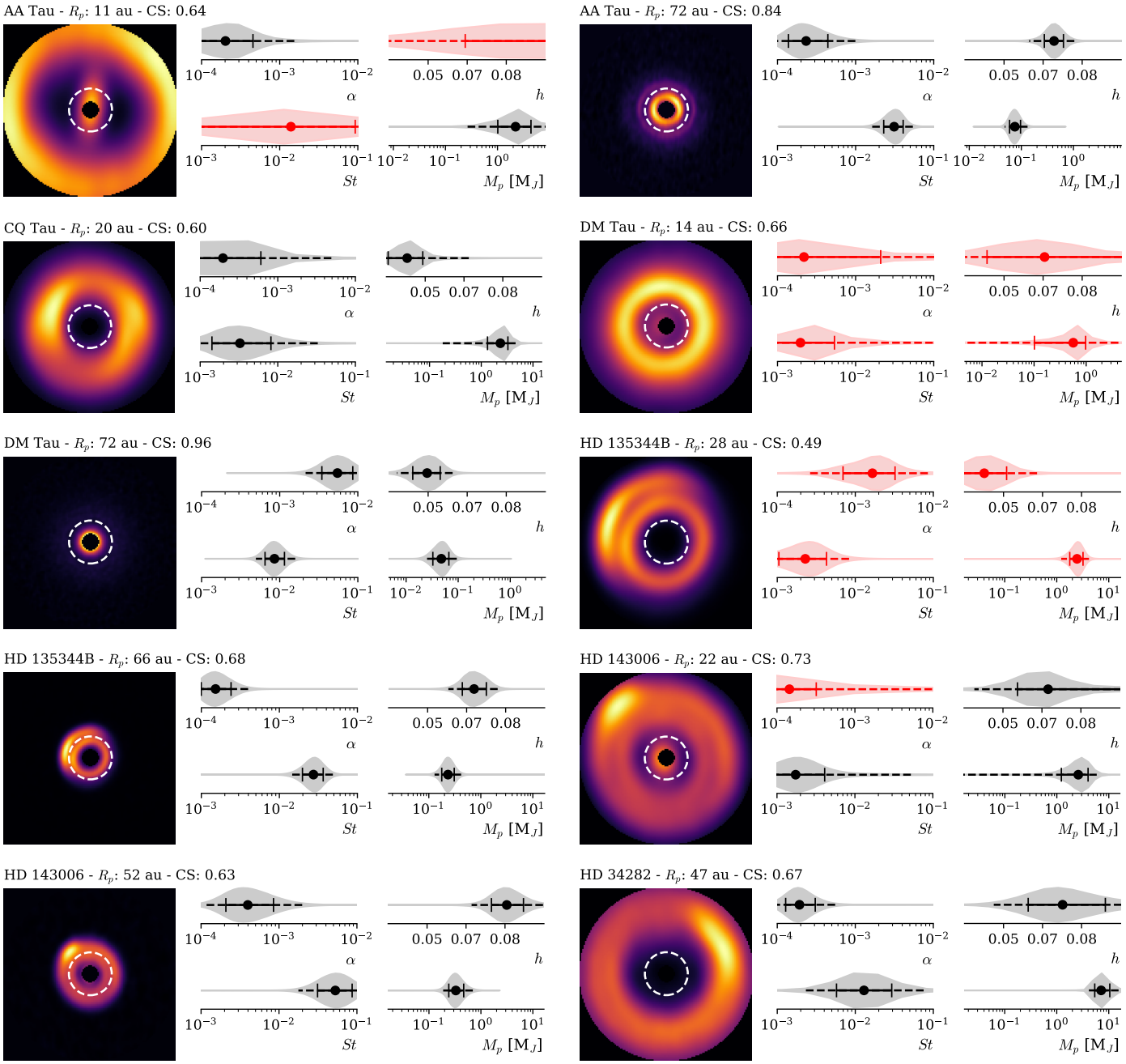


**Figure 12.** First gallery of DBNets2.0 results for the considered sample, which continues in Figure 13. All disk images are shown after deprojection and rescaling. Disk names, fiducial planet positions ($R_p$, marked with the white dashed circle), and CSs are reported in the panels' titles. The violin plots represent DBNets2.0-inferred posterior distributions for each disk and planet property; the continuous error bars inside the violins mark the 16th, 50th, and 84th percentiles, while the dashed lines indicate the range between the 2.5th and 97.5th percentiles. Red violins indicate estimates that do not meet our acceptance criteria, namely CS $> 0.6$ and both the 2.5th and 97.5th percentiles falling within the uniform prior of the respective property.

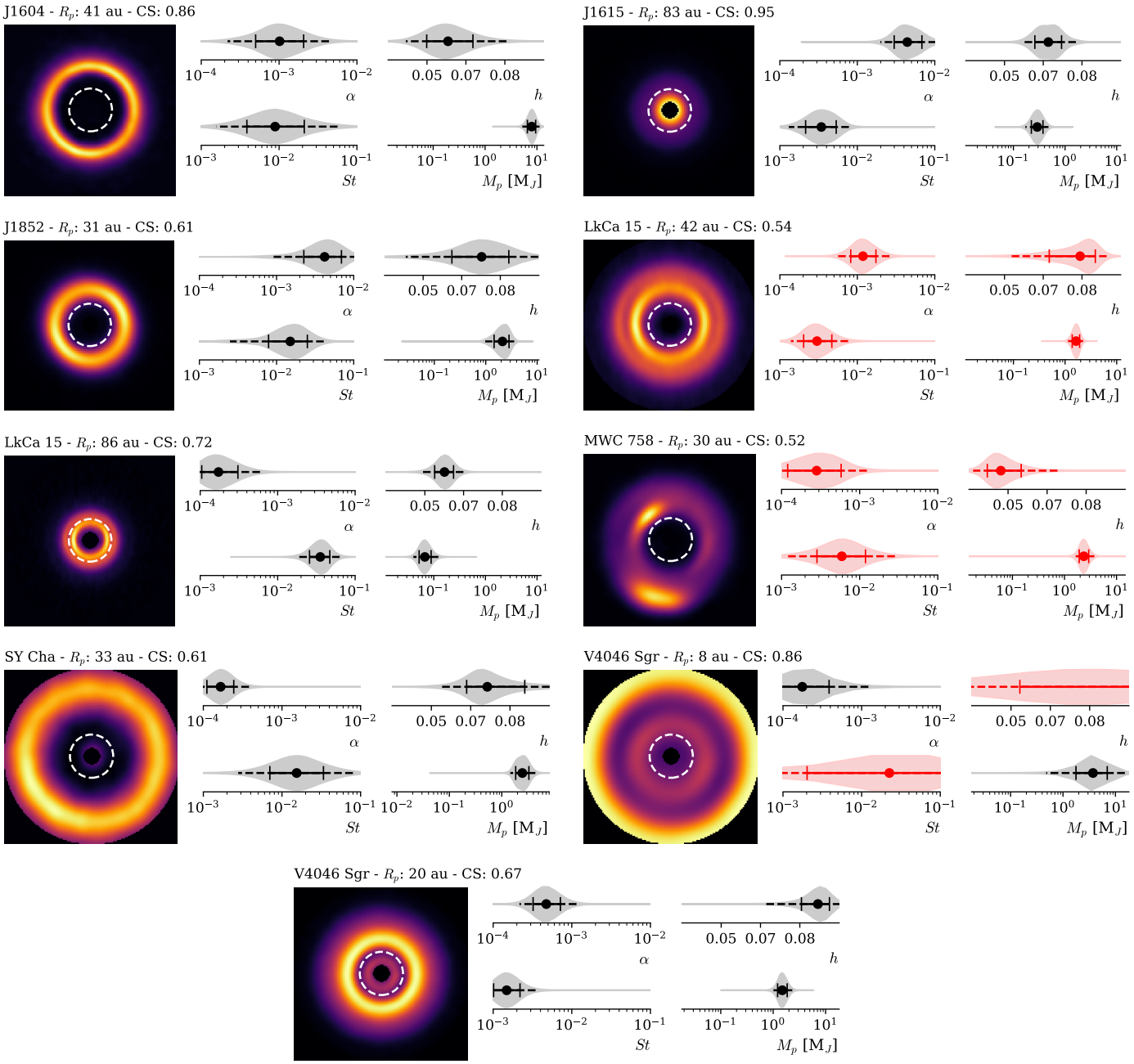


**Figure 13.** Second gallery of DBNets2.0 results for the considered sample, continued from Figure 12. All disk images are shown after deprojection and rescaling. Disk names, fiducial planet positions ($R_p$, marked with the white dashed circle), and CSs are reported in the panels' titles. The violin plots represent DBNets2.0-inferred posterior distributions for each disk and planet property; the continuous error bars inside the violins mark the 16th, 50th, and 84th percentiles while the dashed lines indicate the range between the 2.5th and 97.5th percentiles. Red violins indicate estimates that do not meet our acceptance criteria, namely CS $> 0.6$ and both the 2.5th and 97.5th percentiles falling within the uniform prior of the respective property.

## Appendix E
## Comparison with Estimates in the DBNets2.0 Paper

We showed in Figure 5 a comparison between DBNets2.0 estimates for the planet masses obtained using exoALMA Band 7 observations with those obtained using better resolved, or shorter-wavelength observations, in R25. In Figure 14, we complete this comparison showing the other estimated properties, which we already discussed in Section 5.1.

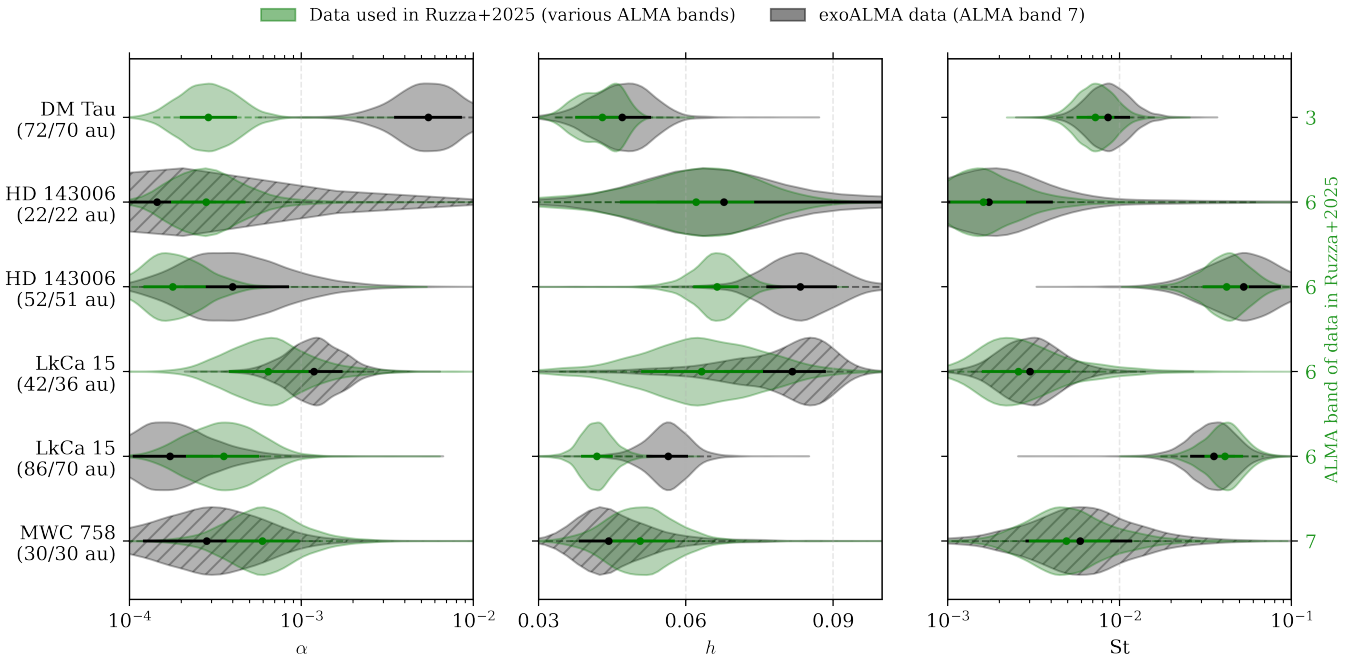


**Figure 14.** Comparison, for the overlapping objects, of DBNets2.0 estimates derived in R25 for archival data (green violins) with those obtained in this work for the exoALMA observations (black violins). On the right, in green, the band of the continuum observation used in R25 is displayed. Near each disk name, we report the assumed planet locations, respectively, in R25 and in this work. Violin plots of unconstrained or unreliable estimates are hatched.

## Appendix F
## Correlations with Other Disk Properties

We checked for correlations of the inferred disk and planet properties with other disk characteristics measured in separate studies, namely the disks' gas-to-dust mass ratio, NAI, and masses of the gas, dust, and host stars. To do that, we selected pairs of properties and computed the Pearson correlation coefficient ($\rho$), whose value indicates the strength and direction of a linear correlation (ranging from $-1$ to $+1$), and evaluated its statistical significance through the corresponding $p$-value. The latter indicates the probability of uncorrelated data to produce a Pearson correlation at least as extreme as the one computed. A $p$-value lower than 0.05 indicates statistically significant evidence for a correlation between the two properties. For this analysis, we remove all estimates that we considered either unreliable or unconstrained. Figure 15 presents the results of this

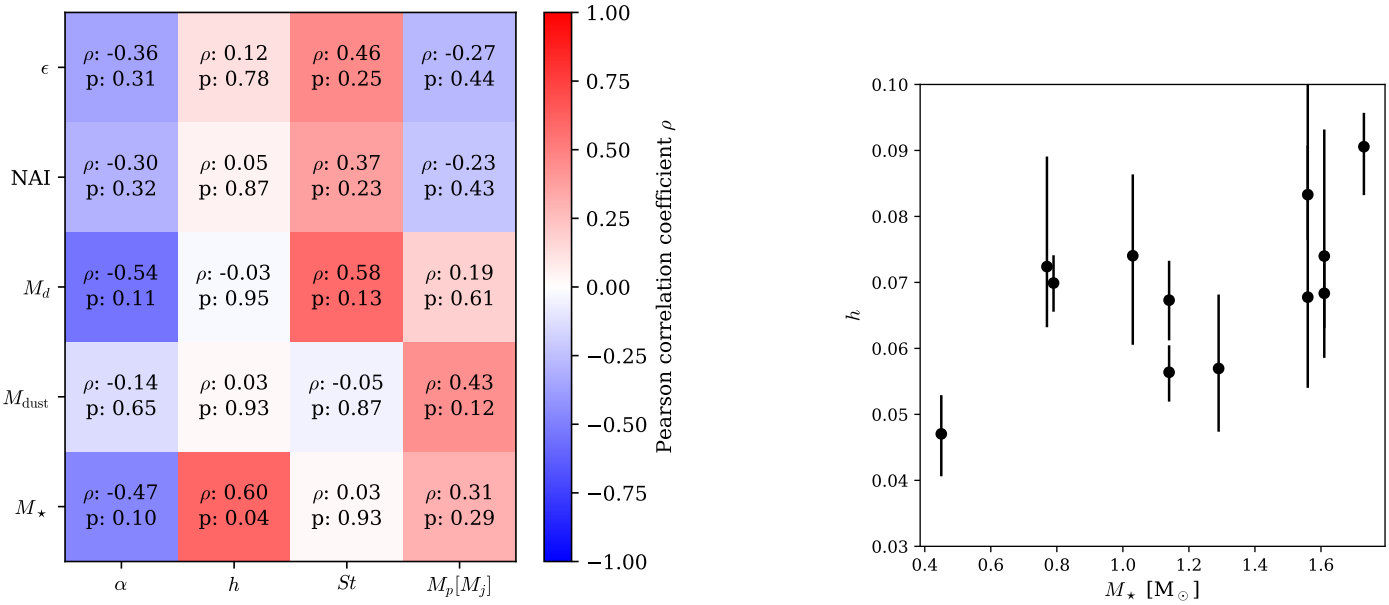


**Figure 15.** Left panel: analysis of correlations between the estimated disk and planet properties with other disk features. Namely, from top to bottom, the disk gas-to-dust mass ratio ($\epsilon$; P. Curone et al. 2025), the disks' NAI (P. Curone et al. 2025), the disk dynamical masses (C. Longarini et al. 2025), the disk dust masses (P. Curone et al. 2025), and the star masses (A. F. Izquierdo et al. 2025). The color bar refers to the Pearson correlation coefficient $\rho$. These are also reported in the plot for each combination of properties, together with the $p$-value corresponding to the null hypothesis of the two properties being independent and normally distributed. Right panel: details of the only statistically significant correlation highlighted by the analysis of Pearson correlation coefficients. This is between the inferred aspect ratios ($h$) and the host star masses.

analysis. We find only one statistically significant correlation between stellar mass and the inferred aspect ratio, which likely arises because more massive stars are more luminous, and thus their stronger irradiation heats the disk, increasing its aspect ratio.

## ORCID iDs

Alessandro Ruzza https://orcid.org/0009-0007-6448-658X
Giuseppe Lodato https://orcid.org/0000-0002-2357-7692
Giovanni Rosotti https://orcid.org/0000-0003-4853-5736
Philip Armitage https://orcid.org/0000-0001-5032-1396
Stefano Facchini https://orcid.org/0000-0003-4689-2684
Sean M. Andrews https://orcid.org/0000-0003-2253-2270
Jaehan Bae https://orcid.org/0000-0001-7258-770X
Marcelo Barraza-Alfaro https://orcid.org/0000-0001-6378-7873
Myriam Benisty https://orcid.org/0000-0002-7695-7605
Pietro Curone https://orcid.org/0000-0003-2045-2154
Daniele Fasano https://orcid.org/0000-0003-4679-4072
Cassandra Hall https://orcid.org/0000-0002-8138-0425
Thomas Hilder https://orcid.org/0000-0001-7641-5235
Andrés F. Izquierdo https://orcid.org/0000-0001-8446-3026
Cristiano Longarini https://orcid.org/0000-0003-4663-0318
François Ménard https://orcid.org/0000-0002-1637-7393
Christophe Pinte https://orcid.org/0000-0001-5907-5179
Jochen Stadler https://orcid.org/0000-0002-0491-143X
Richard Teague https://orcid.org/0000-0003-1534-5186
Jason Terry https://orcid.org/0000-0002-8590-7271
David J. Wilner https://orcid.org/0000-0003-1526-7587
Andrew J. Winter https://orcid.org/0000-0002-7501-9801
Tomohiro C. Yoshida https://orcid.org/0000-0001-8002-8473
Brianna Zawadzki https://orcid.org/0000-0001-9319-1296

## References

Aguayo, A., Caceres, C., Guo, Z., et al. 2025, A&A, 698, A165
Alarcón, F., Bergin, E. A., & Cugno, G. 2024, ApJ, 966, 225
ALMA Partnership, Brogan, C. L., Pérez, L. M., et al. 2015, ApJL, 808, L3
Aly, H., & Lodato, G. 2020, MNRAS, 492, 3306
Andrews, S. M., Huang, J., Pérez, L. M., et al. 2018, ApJL, 869, L41
Asensio-Torres, R., Henning, T., Cantalloube, F., et al. 2021, A&A, 652, A101
Auddy, S., & Lin, M.-K. 2020, ApJ, 900, 62
Auddy, S., Dey, R., Lin, M.-K., & Hall, C. 2021, ApJ, 920, 3
Auddy, S., Dey, R., Lin, M.-K., Carrera, D., & Simon, J. B. 2022, ApJ, 936, 93
Bae, J., Isella, A., Zhu, Z., et al. 2023, ASPC, 534, 423
Bae, J., Flock, M., Izquierdo, A., et al. 2025, ApJL, 984, L12
Ballabio, G., Nealon, R., Alexander, R. D., et al. 2021, MNRAS, 504, 888
Barge, P., Ricci, L., Carilli, C. L., & Previn-Ratnasingam, R. 2017, A&A, 605, A122
Benisty, M., Juhasz, A., Boccaletti, A., et al. 2015, A&A, 578, L6
Benitez-Llambay, P., & Masset, F. S. 2016, ApJS, 223, 11
Bergez-Casalou, C., Bitsch, B., Pierens, A., Crida, A., & Raymond, S. N. 2020, A&A, 643, A133
Birnstiel, T., Dullemond, C. P., Zhu, Z., et al. 2018, ApJL, 869, L45
Calcino, J., Christiaens, V., Price, D. J., et al. 2020, MNRAS, 498, 639
Capelleveen, R. F. v., Ginski, C., Kenworthy, M. A., et al. 2025, ApJL, 990, L8
Casassus, S., Christiaens, V., Cárcamo, M., et al. 2021, MNRAS, 507, 3789
Cazzoletti, P., van Dishoeck, E. F., Pinilla, P., et al. 2018, A&A, 619, A161
Clarke, C. J., Tazzari, M., Juhasz, A., et al. 2018, ApJL, 866, L6
Cranmer, K., Brehmer, J., & Louppe, G. 2020, PNAS, 117, 30055
Curone, P., Facchini, S., Andrews, S. M., et al. 2025, ApJL, 984, L9
Currie, T., Marois, C., Cieza, L., et al. 2019, ApJL, 877, L3
de Boer, J., Ginski, C., Chauvin, G., et al. 2021, A&A, 649, A25
Dempsey, A. M., Muñoz, D. J., & Lithwick, Y. 2021, ApJL, 918, L36
Dipierro, G., & Laibe, G. 2017, MNRAS, 469, 1932
Dipierro, G., Price, D., Laibe, G., et al. 2015, MNRAS, 453, L73
Dipierro, G., Ricci, L., Pérez, L., et al. 2018, MNRAS, 475, 5296
Donati, J.-F., Gregory, S. G., Montmerle, T., et al. 2011, MNRAS, 417, 1747
Dong, R., & Fung, J. 2017, ApJ, 835, 146
Dullemond, C. P., & Penzlin, A. B. T. 2018, A&A, 609, A50
Elbakyan, V., Wu, Y., Nayakshin, S., & Rosotti, G. 2022, MNRAS, 515, 3113
Fairlamb, J. R., Oudmaijer, R. D., Mendigutía, I., Ilee, J. D., & Van Den Ancker, M. E. 2015, MNRAS, 453, 976
Fedele, D., Tazzari, M., Booth, R., et al. 2018, A&A, 610, A24
Flaherty, K., Hughes, A. M., Simon, J. B., et al. 2020, ApJ, 895, 109
Flaherty, K. M., Hughes, A. M., Rosenfeld, K. A., et al. 2015, ApJ, 813, 99
Francis, L., Marel, N. v. d., Johnstone, D., et al. 2022, AJ, 164, 105
Galloway-Sprietsma, M., Bae, J., Izquierdo, A. F., et al. 2025, ApJL, 984, L10
Gardner, C. H., Isella, A., Li, H., et al. 2025, ApJL, 984, 16
Garufi, A., Quanz, S. P., Avenhaus, H., et al. 2013, A&A, 560, A105
Gladman, B., Gladman, & Brett 1993, Icar, 106, 247
Grady, C. A., Muto, T., Hashimoto, J., et al. 2013, ApJ, 762, 48
Guilloteau, S., Dutrey, A., Wakelam, V., et al. 2012, A&A, 548, A70
Gyeol Yun, H., Kim, W.-T., Bae, J., & Han, C. 2019, ApJ, 884, 142
Hammond, I., Christiaens, V., Price, D. J., et al. 2022, MNRAS, 515, 6109
Hardiman, C., Pinte, C., Price, D. J., et al. 2026, ApJL, 997, 47
Hartmann, L., Herczeg, G., & Calvet, N. 2016, ARA&A, 54, 135
Hawley, J. F. 2001, ApJ, 554, 534
Hu, X., Zhu, Z., Okuzumi, S., et al. 2019, ApJ, 885, 36
Huang, J., Andrews, S. M., Dullemond, C. P., et al. 2020, ApJ, 891, 48
Isella, A., Guidi, G., Testi, L., et al. 2016, PhRvL, 117, 251101
Isella, A., Benisty, M., Teague, R., et al. 2019, ApJ, 879, L25
Izquierdo, A. F., Stadler, J., Galloway-Sprietsma, M., et al. 2025, ApJL, 984, L8
Jennings, J., Booth, R. A., Tazzari, M., Rosotti, G. P., & Clarke, C. J. 2020, MNRAS, 495, 3209
Kanagawa, K. D., Tanaka, H., Muto, T., Tanigawa, T., & Takeuchi, T. 2015, MNRAS, 448, 994
Kanagawa, K. D., Muto, T., Tanaka, H., et al. 2016, PASJ, 68, 43
Kanagawa, K. D., Tanaka, H., Muto, T., & Tanigawa, T. 2017, PASJ, 69, 97
Keppler, M., Teague, R., Bae, J., et al. 2019, A&A, 625, A118
Leemker, M., Booth, A. S., Van Dishoeck, E. F., et al. 2022, A&A, 663, A23
Lodato, G., Dipierro, G., Ragusa, E., et al. 2019, MNRAS, 486, 453
Lodato, G., Rampinelli, L., Viscardi, E., et al. 2022, MNRAS, 518, 4481
Long, F., Andrews, S. M., Zhang, S., et al. 2022, ApJL, 937, L1
Longarini, C., Lodato, G., Rosotti, G., et al. 2025, ApJL, 984, L17
Loomis, R. A., Öberg, K. I., Andrews, S. M., & Macgregor, M. A. 2017, ApJ, 840, 23
Loomis, R. A., Facchini, S., Benisty, M., et al. 2025, ApJL, 984, L7
Maio, F., Fedele, D., Roccatagliata, V., et al. 2025, A&A, 699, L10
Manara, C. F., Mordasini, C., Testi, L., et al. 2019, A&A, 631, L2
Manara, C. F., Ansdell, M., Rosotti, G. P., et al. 2023, ASPC, 534, 539
Mao, S., Dong, R., Moo Yi, K., et al. 2024, Disk2Planet: A Robust and Automated Machine Learning Tool for Parameter Inference in Disk-Planet Systems, Tech. rep., https://github.com/smao-astro/PPDONet
Martire, P., Longarini, C., Lodato, G., et al. 2024, A&A, 686, A9
Meru, F., Rosotti, G. P., Booth, R. A., Nazari, P., & Clarke, C. J. 2019, MNRAS, 482, 3678
Mordasini, C., Alibert, Y., Klahr, H., & Henning, T. 2012, A&A, 547, A111
Müller Tobias, W. A., & Kley, W. 2013, A&A, 560, A40
Muto, T., Grady, C. A., Hashimoto, J., et al. 2012, ApJL, 748, L22
Nazari, P., Booth, R. A., Clarke, C. J., et al. 2019, MNRAS, 485, 5914
Öberg, K. I., Guzmán, V. V., Walsh, C., et al. 2021, ApJS, 257, 1
Orihara, R., Momose, M., Muto, T., et al. 2023, PASJ, 75, 424
Papamakarios, G., Pavlakou, T., Murray, I., et al. 2017, arXiv, arXiv:1705.07057
Pinte, C., Price, D. J., Ménard, F., et al. 2020, ApJL, 890, L9
Pinte, C., Ilee, J. D., Huang, J., et al. 2025, ApJL, 984, L15
Reggiani, M., Christiaens, V., Absil, O., et al. 2018, A&A, 611, A74
Ren, B., Dong, R., Esposito, T. M., et al. 2018, ApJL, 857, L9
Ren, B., Dong, R., Holstein, R. G. v., et al. 2020, ApJL, 898, L38
Ribas, A., Vioque, M., Zagaria, F., et al. 2025, NatAs, 9, 1176
Ricci, L., Testi, L., Natta, A., et al. 2010, A&A, 512, A15
Rosotti, G. P. 2023, NewAR, 96, 101674
Rosotti, G. P., Juhasz, A., Booth, R. A., & Clarke, C. J. 2016, MNRAS, 459, 2790
Ruíz-Rodríguez, D., Kastner, J. H., Dong, R., et al. 2019, AJ, 157, 237
Ruzza, A., Lodato, G., & Rosotti, G. P. 2024, A&A, 685, A65
Ruzza, A., Lodato, G., Rosotti, G. P., & Armitage, P. J. 2025, A&A, 700, A190
Scardoni, C. E., Clarke, C. J., Rosotti, G. P., et al. 2022, MNRAS, 514, 5478

Shafaat Mahmud, S., Auddy, S., Turner, N., & Bary, J. S. 2026, ApJ, 997, 225
Shakura, N. I., & Sunyaev, R. A. 1973, IAUS, 55, 155
Sierra, A., Pinilla, P., Perez, L. M., et al. 2025, MNRAS, 538, 2358
Simon, J. B., Hughes, A. M., Flaherty, K. M., Bai, X.-N., & Armitage, P. J. 2015, ApJ, 808, 180
Stadler, J., Benisty, M., Izquierdo, A., et al. 2023, A&A, 670, L1
Stadler, J., Benisty, M., Winter, A. J., et al. 2025, ApJL, 984, L11
Stolker, T., Dominik, C., Avenhaus, H., et al. 2016, A&A, 595, A113
Stolker, T., Kammerer, J., Benisty, M., et al. 2024, A&A, 682, A20
Teague, R., Guilloteau, S., Semenov, D., et al. 2016, A&A, 592, A49
Teague, R., Benisty, M., Facchini, S., et al. 2025, ApJL, 984, L6
Toci, C., Lodato, G., Fedele, D., Testi, L., & Pinte, C. 2019, ApJL, 888, L4
Ubeira Gabellini, M. G., Miotello, A., Facchini, S., et al. 2019, MNRAS, 486, 4638
Uyama, T., Hashimoto, J., Kuzuhara, M., et al. 2017, AJ, 153, 106
Uyama, T., Muto, T., Mawet, D., et al. 2020, AJ, 159, 118
van Terwisga, S. E., van Dishoeck, E. F., Ansdell, M., et al. 2018, A&A, 616, A88
Veronesi, B., Lodato, G., Dipierro, G., et al. 2019, MNRAS, 489, 3758
Veronesi, B., Ragusa, E., Lodato, G., et al. 2020, MNRAS, 495, 1913
Villenave, M., Benisty, M., Dent, W. R., et al. 2019, A&A, 624, A7
Wagner, K., Stone, J. M., Spalding, E., et al. 2019, ApJ, 882, 20
Wallack, N. L., Ruffio, J.-B., Ruane, G., et al. 2024, AJ, 168, 78
Wang, S., Kanagawa, K. D., Suto, Y., et al. 2021, ApJ, 923, 165
Weber, P., Casassus, S., & Perez, S. 2022, MNRAS, 510, 1612
Willson, M., Kraus, S., Kluska, J., et al. 2016, A&A, 595, A9
Wolff, S. G., Perrin, M., Millar-Blanchaer, M. A., et al. 2016, ApJL, 818, L15
Yoshida, T. C., Curone, P., Stadler, J., et al. 2025, ApJL, 984, L19
Zhang, S., Zhu, Z., Huang, J., et al. 2018, ApJL, 869, L47
Zhang, S., Zhu, Z., & Kang, M. 2022, MNRAS, 510, 4473